Volumetric solar heating of nanofluids for direct vapor generation

Citation: Ni, George et al. "Volumetric Solar Heating of Nanofluids for Direct Vapor Generation." Nano Energy 17 (October 2015): 290–301 © 2015 Elsevier Ltd

As Published: http://dx.doi.org/10.1016/j.nanoen.2015.08.021

Publisher: Elsevier

Persistent URL: http://hdl.handle.net/1721.1/111647

Version: Author's final manuscript: final author's manuscript post peer review, without publisher's formatting or copy editing

Volumetric Solar Heating of Nanofluids for Direct Vapor Generation

George Ni[a], Nenad Miljkovic[a,1], Hadi Ghasemi[a,2], Xiaopeng Huang[a], Svetlana V. Boriskina[a], Cheng-Te Lin[a,3], Jian Jian Wang[a], Yanfei Xu[a], Md. Mahfuzur Rahman[b], TieJun Zhang[b], and Gang Chen[a,*]

Affiliation Addresses:

[a]*Department of Mechanical Engineering, Massachusetts Institute of Technology, 77 Massachusetts Ave, Cambridge, Massachusetts 02139*

[b]*Department of Mechanical and Materials Engineering, Masdar Institute of Science and Technology, Masdar City, Abu Dhabi, United Arab Emirates*

Present Addresses:

[1]*Department of Mechanical Science and Engineering, University of Illinois, Urbana, Illinois, 61801, USA*

[2]*Department of Mechanical Engineering, University of Houston, Houston, Texas, 77204, USA*

[3]*Key Laboratory of Marine New Materials and Related Technology, Zhejiang Key Laboratory of Marine Materials and Protection Technology, Ningbo Institute of Material Technology & Engineering, Chinese Academy of Sciences, Ningbo, 315201, China*

* Address post-published correspondence to: gchen2@mit.edu

Address refereeing and publishing correspondence to: georgeni@mit.edu

Abstract

Traditional solar-thermal receivers suffer from high surface temperatures, which increase heat losses to the surroundings. To improve performance, volumetric receivers based on nanoparticles suspended in liquid (nanofluids) have been studied as an approach to reduce surface losses by localizing high temperatures to the interior of the receiver. Here, we report measured vapor generation efficiencies of 69% at solar concentrations of 10 suns using graphitized carbon black, carbon black, and graphene suspended in water, representing a significant improvement in both transient and steady-state performance over previously reported results. To elucidate the vapor generation mechanism and validate our experimental results, we develop numerical and analytical heat transfer models that suggest that nanofluid heating and vapor generation occur due to classical global heating of the suspension fluid. This work demonstrates high nanofluid-assisted vapor generation efficiencies with potential applications in power generation, distillation, and sterilization.

Keywords: nanofluid, vapor generation, steam generation, solar energy, nanoparticle, volumetric receiver

1. Introduction

Traditional solar-thermal receivers consist of surface absorbers that convert the majority of the incoming solar radiation into heat while minimizing thermal re-radiation loss.[1-12] Although these receivers have high photothermal conversion efficiencies, surface absorbers are ill-suited for heating carrier fluids because the heat generation is separated from the fluid to be heated. At high solar concentrations (>50 suns), such as those used in industrial-scale solar thermal power plants,[13-21] a large temperature difference forms between the absorber and the fluid, leading to high surface temperatures and high radiative losses. One approach to minimizing the absorber-to-fluid temperature difference is to use volumetric absorption within the carrier fluid itself, which has been predicted to lead to a 5-10% increase in photothermal efficiency.[17,22,23] Volumetric absorbers such as porous media,[24-29] gas-particle suspensions,[22,30-34] molten salts,[1,6] and nanoparticles suspended in fluids (nanofluids)[13,15-21,35,36] have been used to minimize surface temperatures of receivers, thereby reducing the receiver heat losses. Volumetric absorbers can have surface temperatures lower than even the bulk fluid temperature,[17,36,37] otherwise known as thermal trapping.[24,26,38]

Recently, nanofluids have been introduced as an attractive approach to direct steam generation using solar energy *via* nanoparticle absorption.[22,30,32,34,37,39] In addition, nanofluids have been shown to enhance critical heat flux in certain boiling applications.[40,41] Neumann *et al.* demonstrated the use of nanofluids for direct water vapor generation,[6,42] reaching device efficiencies of 24% at solar concentrations of 1000 suns (1 sun = 1 kWm^{-2}). Although a novel approach, the exact mechanism of vapor generation has been debated over the past few years.[6,35,36] Two potential mechanisms have been proposed to explain the vapor generation results.[36,37,43]

In one mechanism, nanoparticles isolate the heat generation to very near the particle-liquid interface in a non-equilibrium manner such that the surrounding bulk fluid remains cold while the particle heats up to a temperature which nucleates a vapor bubble locally. Several researchers have studied nanoscale-to-microscale bubble formation surrounding individual and arrayed nanoparticles. Lukianova *et al*. conducted pulse-laser illumination of gold nanoparticles to show that a critical laser fluence equivalent to $3x10^8$ suns was required before bubble formation initiated.[20,38,43-45] Fang *et al*, performed continuous laser illumination experiments of gold nanoparticles on a substrate and observed a similarly high nanobubble formation intensity threshold, on the order of $3x10^7$ suns.[37,46] Lombard *et al*. modeled theoretically the kinetics of nanobubble formation around gold nanoparticles,[36,42] showing that an intensity of $\sim 1x10^{10}$ suns was required to nucleate a bubble. Though nanobubble formation has been observed, a combined optical absorption and heat conduction model using achievable illumination intensities does not give the required temperature differential.[6,47,48]

In the second mechanism, nanoparticles rapidly reach equilibrium with the surrounding fluid, and vapor generation is purely due to the rise in temperature of the bulk fluid.[2,36,43,49,50] Several experiments have shown that the interparticle fluid temperatures can reach as high as the spinodal decomposition temperature of water (594 ± 17K) before bubble formation.[20,43-45,51] In addition, Keblinski and Cahill simulated an array of 5000 nanoparticles, and found that two time scales exist in the heating profile of nanofluids.[46,52] They found that heating on the macroseconds scale is due to global heating of the fluid, but on the nanoscale the heating is confined near to the nanoparticle. Finally, a recent work by Hogan *et al* has focused on using high intensity lasers ($\sim 10^6$ W/m^2) to show the effect of light scattering leading to localized absorption on the direct vapor generation from nanofluids. They simulated light propagation through the nanofluid, and compared experimentally with nanoparticles of varying scattering cross sections. In their work, they concluded that Fourier-law heat conduction adequately describes the nanoparticle-based direct steam generation.[2,36]

Based on the previous studies, there exists a need to 1) increase the efficiency of the direct solar vapor generation process to make the technology more competitive with existing solar vapor generation techniques,[6,47,48] 2) seek solutions that utilize the full spectrum of solar energy at lower optical concentrations (≤10 suns) than previous work to achieve commercial viability and minimize system cost,[2,49,50,53] and 3) gain a better understanding of the physical mechanisms governing solar vapor generation. Through rational design and detailed experiments, we show highly efficient direct vapor generation (69±4% at 80°C). We attain these results using water based nanofluid solar receivers at low optical concentrations (≤10 suns), in comparison to all previous work, which used high intensity lasers or high optical concentration solar flux. A solar concentration of 10 suns is approximately the highest achievable without active sun-tracking, *via* non-imaging optics.[51,54] In some concentrated solar plants (CSP) the optical collection field can comprise up to 30% of the total installed cost.[52,55] In addition, we report that well-dispersed nanofluids can lead to higher vapor generation in transient conditions. Furthermore, through a consistent set of numerical simulation, analytical modeling, and experimental validation, we clarify that the solar vapor

generation of nanofluids is in fact due to global heating of the bulk fluid and related classical evaporation phenomena. This work advances a direct solar vapor generation platform that promises to be low cost and has potential for a wide-range of solar-based applications such as power generation,[2,56] distillation,[6,32] and sterilization.[53,57]

2. Methods and Materials

To study the effect of different nanofluids on the receiver efficiency, we performed solar vapor generation experiments on a custom-built lab-scale receiver. To supply solar energy to the nanofluid samples, a solar simulator was used in conjunction with a Fresnel lens and aperture to generate and focus concentrated solar light (Fig.1a). The nanofluid container was constructed out of two concentric acrylic tubes, with a layer of aerogel particles in between to serve as an insulator to minimize radial heat losses (Fig.1b). The aerogel particles were sealed from the environment with acrylic discs. The nanofluid was exposed to the ambient to vent the vapor. No insulation was used over the top of the nanofluid, which maximized the evaporation efficiency by allowing faster vapor diffusion. Four E-type thermocouples were inserted into the nanofluid container to measure the fluid temperature at different distances from the nanofluid-air interface. As the nanofluid evaporated, the fluid level dropped below each thermocouple, allowing temperature measurement of the liquid-vapor interface location. The mass loss was measured using a high accuracy weight scale (see Supporting Information, section S1).

Carbon based nanoparticles are significantly lower cost than metal nanoparticle suspension, and have better broadband solar absorptance.[58] Three different highly absorbing nanofluids were synthesized for this work: graphitized carbon black (GCB, Fig.1c), carbon black (CB, Fig.1d), and graphene particles suspended in water (Fig. 1e). The nanofluids were created by sonicating 0.5 wt% of the various nanoparticles in distilled water for 1 hour. We chose the nanoparticle concentration to be 0.5wt % based on previous works in studying the effect of nanoparticle fraction on photothermal properties of nanofluids.[58] The GCB (Sigma-Aldrich, 699632-25G <500nm) and CB (Cabot, Vulcan 9 N110) were commercially purchased. The graphene nanosheets were made using an electrochemically stimulated exfoliation process.[6,54] All three nanofluids appeared stably suspended throughout the duration of the test. During storage, the GCB nanofluid was stable for months at a time, whereas the graphene nanofluid was stable for over a year. The CB nanofluid was stable for periods less than a week.

To study the non-constant nature of solar irradiance during the day, both steady-state and transient receiver efficiencies were measured.

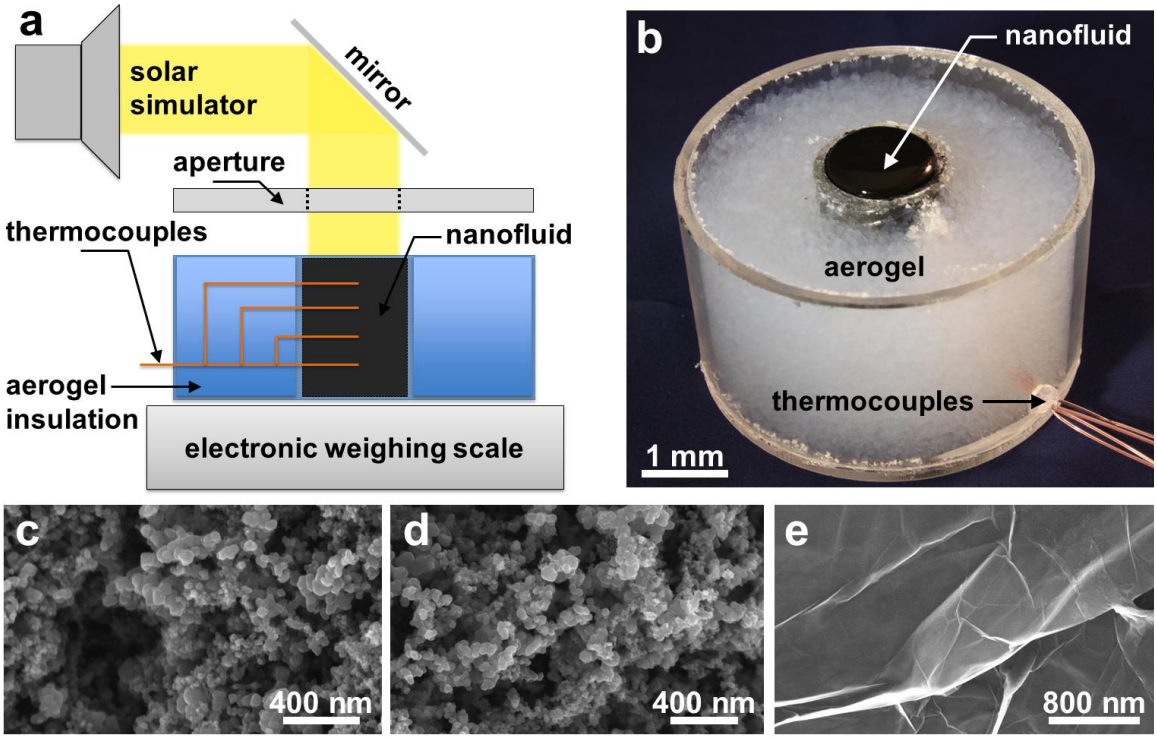

Figure 1. (a) Schematic of solar vapor generation device. (b) Image of the nanofluid container showing the aerogel insulation, black nanofluid, and thermocouple feed through. Scanning electron micrographs (SEM) of (c) graphitized carbon black, (d) carbon black, and (e) graphene nanoparticles. To obtain SEM images, the nanofluids were dehydrated prior to imaging.

The small cuvette measurements (Lumped Capacitance Model, Fig.6) consisted of a rectangular transparent cuvette (Plastibrand, PMMA) with dimensions 12.5mm x 12.5mm x 45mm (L x W x H). The cuvette was filled with GCB nanofluid, illuminated from the side with the solar simulator. Three E-type thermocouples (Omega Engineering, TT-E-40-SLE-50) inserted through the cuvette walls measured the nanofluid temperature at different heights in the cuvette. One additional thermocouple is placed above the liquid-vapor interface, and is shielded from direct illumination with aluminum foil. Various solar concentrations were used (1-10 kWm^{-2}), and the temperatures were recorded until steady state was reached. For additional information about the small cuvette experiment, see Supporting Information, section S2.

3. Results

Figure 2 shows the experimental mass change of the nanofluid container as a function of time for each of the studied nanofluids at 10 sun illumination. The absolute mass change rate ($|dm/dt|$) started at zero and gradually increased with time due to the photothermal conversion of solar radiation to enthalpy of evaporation. As the nanofluid absorbed more solar radiation, the temperature of the bulk nanofluid solution gradually increased in conjunction with the evaporation rate. After an initial heating period of ≈4000 seconds, the system reached steady-state operating conditions where the evaporative and parasitic heat losses balanced the absorbed solar radiation. The evaporation efficiency at steady-

state conditions was determined by dividing the gained enthalpy in the generated vapor by the total incoming solar radiation input,

$$\eta = \frac{\dot{m} h_{fg}}{Q_S A}, \quad (1)$$

where $\dot{m}$ is the steady-state vapor mass flux, h_{fg} is the latent heat of vaporization for water at 1 atm (2.257 $MJkg^{-1}$), A is the area of the aperture (4.95 cm^2), and Q_S is the total incoming solar flux (10 kWm^{-2}) after concentrating optics, hence the efficiency reported is an internal efficiency. The steady-state efficiency was determined by using the data where the mass loss is linear to within an R^2-value of 0.999. Although the addition of nanoparticles to water has been reported to change the thermophysical properties such as heat capacity[51,55] and thermal conductivity,[56,59,60] the small concentration of nanoparticles used in this study (0.5 wt%, 0.23 vol%) was determined to have a negligible effect on both properties.[32,61]

The system evaporates nanofluids similarly to a continuous process. The addition of replenishing fluid would add two details to our analysis: 1) conduction of heat to the underlying and flowing liquid, and 2) use of some of the absorbed solar energy to heat the nanofluid up to operating temperature (sensible heating). The receiver had already reached within 2% of steady-state evaporation, while thermocouples showed the underlying liquid to be near room temperature (<30°C). This shows that conduction into the liquid is not a dominant heat loss mechanism. The sensible heat increase in the generated vapor phase ($\dot{m} c_p \Delta T$) was small (~7%) compared to the latent heat of vaporization ($\dot{m} h_{fg}$), and was purposely excluded to conservatively estimate the efficiency.

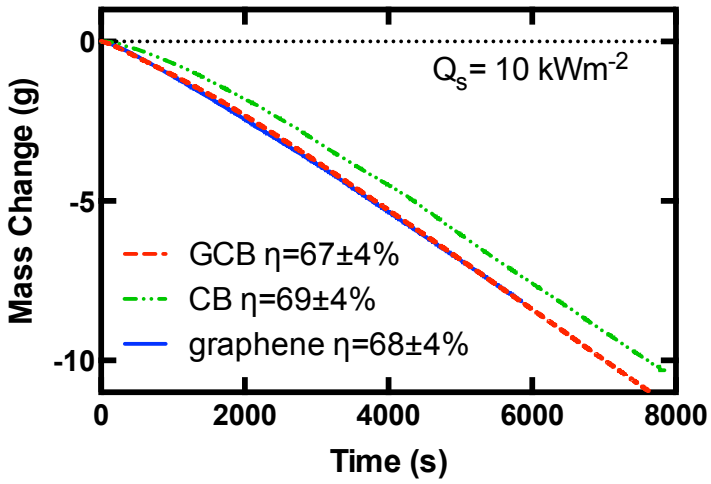

Figure 2. Nanofluid receiver mass change as a function of time for the carbon black (CB), graphitized carbon black (GCB), and graphene nanofluids while illuminated by 10 suns of radiation (Q_s = 10 kWm^{-2}). At steady-state (t > 4000s) the mass change rate was approximately equal for all of the nanofluids ($dm/dt = \dot{m} \approx$ -1.5x10^{-3} gs^{-1}).

The steady-state evaporation efficiency was approximately the same for all three nanofluids tested ($\eta \approx 69\%$), with all calculated values being within the measurement uncertainty (±4%). Of the losses from our system, radiation was calculated to be 4%. The measured specular reflectivity of the nanofluids was <1% (see Supporting Information, section S5). The losses into the container were modeled using a COMSOL simulation and matching the boundary conditions to the embedded thermocouples. The conduction into the bulk underlying nanofluid was ≈9%, and the losses to the surrounding aerogel insulation and ambient were ≈12%. The air convection from the evaporating nanofluid surface accounted for ≈3% of the total losses (see Supporting Information, section S3). Transmission losses were not present for the nanofluids studied here due to all of the incoming radiation being absorbed prior to reaching the bottom of the nanofluid container.

It is important to note that the 69% efficiency includes the incident power on the receiver, but not the losses from the optics. If a Fresnel lens with modest optical efficiency of ≈83% were used to supply concentrated solar light,[57,62] a system vapor generation efficiency of 57% would be achieved. Even with the additional optics loss included, our reported vapor generation efficiency of 57% is higher than achieved in a previous study (≈24%).[6,57] In addition, our nanofluids-based receiver utilized a much lower solar concentration (10x vs. 1000x), one achievable with less stringent tracking requirements and lower cost components.[36,51]

Since the measured steady-state efficiencies for each nanofluid were approximately identical, it can be inferred that the global absorptance of the different nanofluids are similar. Furthermore, the high steady-state vapor conversion efficiency shown here can be attributed to the high absorptivity of the nanofluid in the solar spectrum, and the

unrestricted vapor extraction. In addition, the utilization of low thermal conductivity aerogel insulation (~0.02 $Wm^{-1}K^{-1}$) helped to minimize side loses and allow for a majority of the photothermal energy conversion to be utilized for water phase change. In a larger application-scale nanofluids-based solar receiver, the side losses would be smaller than in the lab-scale device due to a lower surface-to-volume ratio, and even higher efficiencies are potentially achievable.

To examine the transient performance of the nanofluid receiver, we compared the mass change on a smaller time scale ($0 < t < 300$s). Each of the nanofluids was first measured under dark conditions for 10 minutes, to ensure that the nanofluid temperature was consistent with the lab ambient temperature. The cover was removed from the aperture, and data acquisition was initiated. Figure 3(a) shows the mass loss as a function of time during the transient period for the three nanofluids. The GCB-based nanofluid evaporated the most water during the transient period (≈0.3 ± 0.001 g), followed by the graphene (≈0.22 ± 0.001 g) and regular CB nanofluids (≈0.1 ± 0.001 g). The transient performance of the nanofluids was related to how well-dispersed the nanoparticles in the fluids were. The CB nanofluid was noticeably less well-dispersed, and the meniscus was more transparent with particle agglomerates discernible by eye. Nanofluids with well-dispersed particles generated heat closer to the liquid-vapor interface, and had a higher interfacial temperature and overall evaporation rate. The nanofluid dispersity is shown later to be related to the extinction coefficient of the nanofluid. The reason for the variable nanofluid dispersions is due to the different zeta potentials of the nanoparticles in the water solution, which is related to nanofluid stability. Nanofluids with high magnitude of zeta potential (negative or positive) are electrostatically stabilized, while nanofluids with low magnitude zeta potentials tend to agglomerate.[59,60,63] CB nanofluids have been reported to have a zeta potential of only ≈-10 mV,[61,63,64] resulting in agglomeration and lack of stability, while the graphene and GCB nanofluids reportedly have lower zeta potentials (higher magnitude, ≈ -40mV),[36,62] resulting in better nanofluid stability, less agglomeration, and enhanced transient performance.

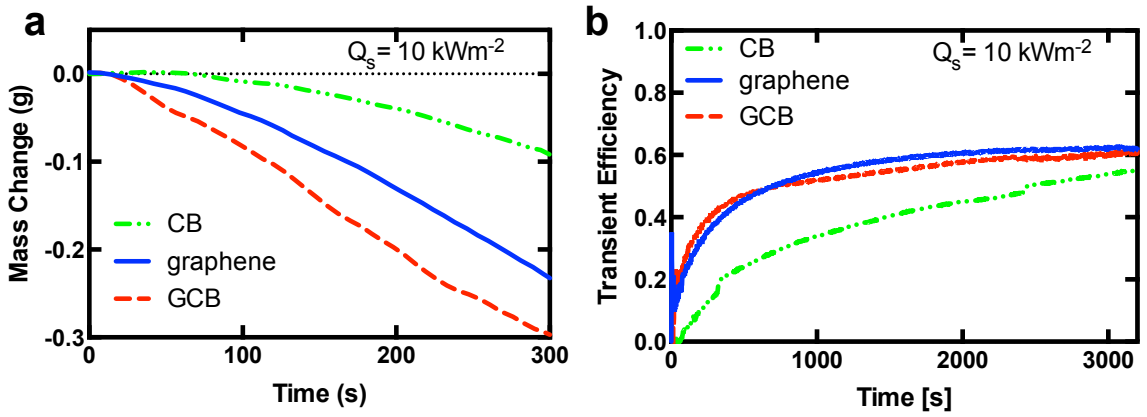

Figure 3. (a) Mass change in transient conditions and (b) transient efficiency as a function of time for the CB, GCB, and graphene nanofluids while illuminated by 10 suns of solar radiation (Q_s = 10 kWm^{-2}). The GCB-based nanofluid had the highest transient evaporation efficiency, followed by the graphene and regular CB nanofluids.

To quantify the transient performance in terms of vapor generation efficiency, we define a transient efficiency, η_T, as the total amount of water evaporated since illumination began divided by the total solar energy incident on the nanofluid receiver during that time interval,

$$\eta = \frac{\int_0^t \dot{m}\left(h_{fg}+c_{p,l}\Delta T\right)dt}{\int_0^t Q_s A dt}, \quad (2)$$

where $c_{p,l}$ is the specific heat of liquid water (4.19 $kJkg^{-1}K^{-1}$), and ΔT is the temperature rise of the liquid prior to evaporation. The transient efficiency depends on the temporal length of the measurement, but is appropriate when considering varying solar power over the course of the day. Despite the GCB nanofluid reaching steady-state faster (Fig.3a), the graphene nanofluid reaches a similar transient efficiency (69±4% for $0 < t < 6000$s). The transient efficiencies of GCB and graphene nanofluids are 7% higher than that of CB nanofluid. At shorter measurement times, this transient efficiency discrepancy increases as shown in Fig.3b. The measured transient receiver efficiency of 69±4% can again be coupled with a modest Fresnel lens optical efficiency of 83%,[57,65] giving a system transient vapor generation efficiency of 57%.

It is important to note that the identical steady-state performance does not indicate that all three nanofluids will achieve the same performance in a given solar application. The transient performance becomes crucial when choosing nanofluids for applications that may have intermittent interruptions in illumination such as rolling cloud cover. Another situation where transient performance becomes important is cases where solar tracking is not used, such as in residential homes. In these cases the solar illumination angle is constantly changing, and therefore the incoming radiation is changing throughout the course of the day. In the case of transient incoming solar radiation, the GCB nanofluid would perform the best due to its ability to reach steady state the fastest and generate the most vapor in the transient period of operation.

4. Transient Efficiency Model

To explain the transient absorption mechanism, we developed an analytical heat transfer model to show that the transient efficiency is dependent on the extinction coefficient of the nanofluid, which is determined by the absorption and scattering characteristics of nanoparticles and their agglomerate size (r_o). A previous study of nanofluids based on metal nanoparticles has shown a positive correlation between the nanoparticle extinction coefficient and nanofluid evaporation rates.[36,65] Since all the nanoparticles are carbon based, we mainly consider the effect of the agglomerate sizes, which were experimentally measured using optical characterization methods, and the dependence of calculated evaporation flux on the extinction coefficient was determined using the developed analytical model.

The nanoparticle agglomerate sizes were determined using dynamic light scattering (DLS) and optical microscopy, depending on the agglomerate size. The GCB

nanoparticles were well dispersed, and had smaller agglomerates (r_o~110 nm) suitable for DLS measurement. The CB nanoparticles are less well dispersed, and their agglomerates were larger (r_o ~5 μm) and observable with optical microscopy (see Supporting Information, section S6). The agglomerate sizes determined the particle density in the nanofluids, since the volume fractions were the same.

Once the nanoparticle agglomerate sizes were determined, an extinction coefficient was calculated for GCB and CB nanofluids, using Mie theory in the independent scattering regime,[63,66] and indices of refraction from literature (see Supporting Information, section S6).[63,64,67] The calculated scattering and absorption cross sections of nanoparticle agglomerates were of similar magnitudes. To approximate the heat generation, the total extinction coefficient calculated was used in the heat generation term for Eq.3 in our transient efficiency model shown later. In the event that forward scattering dominates back scattering, as is the case with the studied nanoparticle agglomerates, our calculations will under predict the difference in transient efficiency. Figure 4. shows the calculated efficiency factors $Q_{ext}, Q_{abs}, Q_{sca}$ for extinction, absorption, and scattering. Using the efficiency factors, the extinction coefficients for GCB and CB were calculated and found to differ more than two orders of magnitude. The estimated extinction coefficients for GCB and CB nanofluids were $5.6\text{x}10^{5}$ m^{-1} and $1.6\text{x}10^{3}$ m^{-1} respectively. Again, the difference in extinction coefficients is largely due to the particle (agglomerate) number density, which given a same amount of material is related to the stability of the suspension.

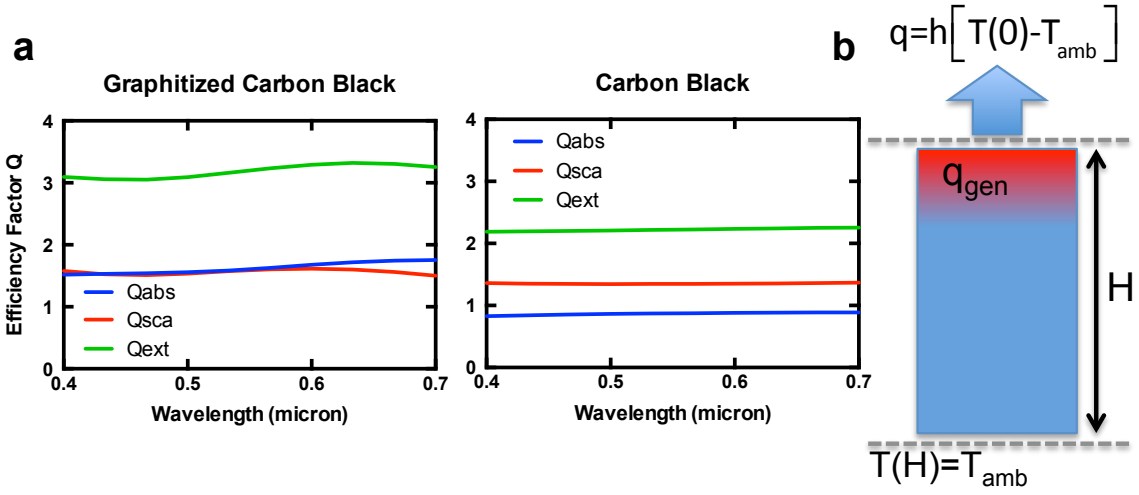

Figure 4. (a) Efficiency factors for the nanoparticles calculated using Mie theory. $Q_{ext}, Q_{abs}, Q_{sca}$ are the efficiency factors for extinction, absorption, and scattering. The carbon black has a smaller extinction efficiency than the graphitized carbon black. (b) A visual schematic of the transient efficiency model.

Using the estimated extinction coefficients of the nanofluids, we constructed an analytical heat transfer model of the nanofluid receiver to determine the effect of extinction

coefficient on the transient performance. Our model neglects convection and considers transient conduction effects coupled with absorption. Only conduction is considered because the heat generation occurs at the top end of the receiver, thereby minimizing natural convection inside. The weaker extinction coefficient shifts the heat generation deeper into the nanofluid receiver, and reduces the temperature of the nanofluid-air interface. This ultimately reduces the evaporation efficiency of the device. A schematic of the transient efficiency heat transfer model can be seen in Fig. 4c. The analytical model is shown in Eq. 3, where λ is an exponential constant for heat generation, and q_0 is the incident light intensity.

$$\frac{\partial \Theta(x,t)}{\partial t} = \alpha_x \frac{\partial^2 \Theta(x,t)}{\partial x^2} + \frac{q_0 \lambda e^{-\lambda x}}{\rho c_p} \tag{3}$$

$$\text{Boundary Condition \#1: } \Theta(H,t) = 0$$

$$\text{Boundary Condition \#2: } -k_x \frac{\partial \Theta(0,t)}{\partial x} + h\Theta(0,t) = 0$$

$$\text{Initial Condition: } \Theta(x,0) = 0$$

The boundary and initial conditions for the heat transfer model are: 1) convectively cooled temperature bath on one end (the evaporation side, $x = 0$), with h ($150 \frac{W}{m^2 K}$) fitted from the COMSOL simulation of the nanofluids receiver, and 2) constant ambient temperature at the other side ($x = H$), and 3) initially, the nanofluid receiver is at ambient temperature. The model is solved using the Green's function method. The results of the simulation are shown below in Fig.5.

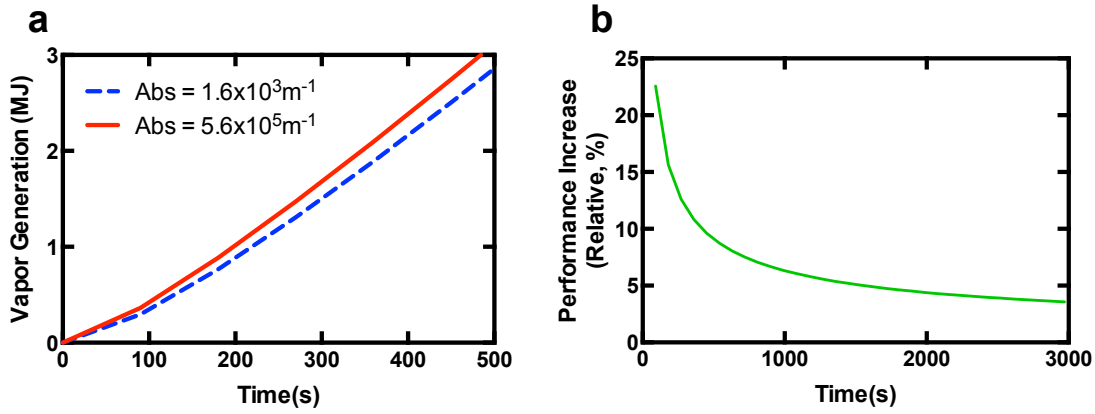

Figure 5. (a) The calculated energy loss through evaporation plotted as a function of time, for nanofluids with different extinction coefficients. The higher extinction coefficient leads to higher evaporation flux due to heat localization at the nanofluid-air interface and higher surface temperature. (b) The relative vapor generation increase in total evaporated energy between the nanofluids considered in (a).

Figure 5a shows the calculated total water vapor generated from the nanofluid as a function of time for the GCB and CB nanofluids. It can be seen that the nanofluid with the larger extinction coefficient (GCB) has the higher vapor generation rate. To help quantify the performance difference between the two nanofluids, Fig.5b shows the relative vapor generation increase between the two nanofluids, which is defined below.

$$\boldsymbol{\eta_{relative} = \frac{h\Theta_{GCB}(0,t)}{h\Theta_{CB}(0,t)}}, \tag{4}$$

where η_{relative} is the relative performance increase of the GCB nanofluid over the CB nanofluid. The performance increase is particularly significant shortly after illumination, and decreases over time. At 3000 seconds, the total vapor generated for the two nanofluids differs by about 4%. This is smaller than the experimentally measured relative difference of 10% in the transient receiver efficiency (Fig.3). We attribute this discrepancy to the use of a constant heat transfer coefficient in the model, whereas in reality the evaporation rate will increase non-linearly with temperature. This is due to the non-linear dependence of vapor pressure, the driving force for evaporation, on temperature. Nonetheless, the experimental and model results show good agreement. This analytical model shows how heat localization due to a larger effective extinction coefficient in the nanofluid can increase the transient evaporation, corroborating recent work on metal particles[36,68] , but does not clarify the mechanism for vapor generation.

5. Horizontal Illumination: Lumped Capacitance Model

To provide insight into the experimental results, and support the mechanism of global fluid heating for vapor generation in these nanofluids, we conducted additional experiments and developed the corresponding model (see Supporting Information section S2). We show from the experiments and model that the evaporation heat transfer coefficients developed to model the evaporation of pure water can also be used to describe the evaporation behavior of nanofluids. We illuminated the nanofluids from the side to achieve uniform temperatures throughout the nanofluid. This allows us to utilize the lumped capacitance approximation in the model. The following assumptions were made: 1) the fluid is isothermal throughout the cuvette ($Bi = \bar{h}L/k_w \approx 0.1$, where Bi, $\bar{h}$, L, and k_w are the Biot number, external heat transfer coefficient to air ($\bar{h} \approx 5$ $\text{Wm}^{-2}\text{K}^{-1}$), thickness length scale of the cuvette ($L \sim 10$ mm), and nanofluid thermal conductivity ($k_w \approx 0.6$ $\text{Wm}^{-1}\text{K}^{-1}$), respectively. 2) The boundary condition at bottom of the cuvette was considered insulated. 3) The side walls are modeled as heated vertical plates undergoing natural convection to the surrounding ambient air,[65,69,70] and radiative losses. 4) The top evaporating surface undergoes both natural convection and evaporation.[65] 5) All incident solar radiation is absorbed by the nanofluid ($\varepsilon \approx 1$). The high solar absorption was validated by measuring the transmission of solar light through a nanofluid filled cuvette using a UV-VIS spectrophotometer (see Supporting Information, section S5).

It is important to note that although our transient efficiency model showed that the fluid temperature is in fact non-uniform and dependent on the extinction coefficient, the

assumption of lumped capacitance in this model is still valid, due to the different illumination conditions. Furthermore, this model is not meant to further elucidate or resolve the transient performance discrepancy from sample to sample, but rather to give a physical picture of the vapor generation process in terms of a global energy balance and validate the classical heat loss mechanisms present in the experiment.

Accounting for all of the heat transfer pathways, the differential equation for the bulk nanofluid temperature, T is (for full derivation, please see Supporting Information, Section S2)

$$\rho_w c_p V \frac{dT}{dt} + \rho_w c_p T \frac{dV}{dt} = q - \left(\overline{h_s} A_s + \overline{h_t} A_t\right)(T - T_\infty) - \varepsilon\sigma A_T\left(T^4 - T_\infty{}^4\right) - \overline{h_e} A_t\left(P(T) - \varphi P(T_\infty)\right), \quad (5)$$

where ρ_w is the nanofluid density (≈1000 kgm^{-3}), V is the nanofluid volume, q is the radiative heat input from the solar simulator (1 kWm^{-2}), $\overline{h_s}$ and $\overline{h_t}$ are the side and top cuvette surface natural heat transfer coefficients, respectively, $\overline{h_e}$ is the evaporation coefficient,[66] A_s, A_t, and A_T are the cuvette side, top, and total surface areas, respectively, T_∞ is the ambient air temperature (T_∞ = T_{amb} ≈ 24°C), $P(T)$ is the water saturation pressure at the bulk nanofluid temperature, φ is the relative humidity, and $P(T_\infty)$ is the water saturation pressure at the ambient temperature.

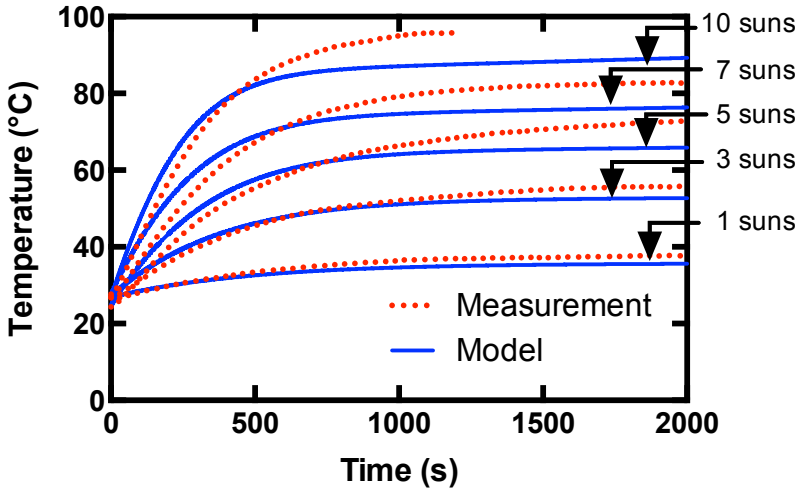

Figure 6. Graphitized carbon black nanofluid temperature as a function of time for 5 different solar concentrations. The experimental results are shown in red solid lines, while the analytical model results (Eq. 5) are shown in blue dotted lines. The bulk fluid temperature was calculated by calculating the arithmetic mean of the four thermocouple probes in the nanofluid. The experimental error in the thermocouple measurement is approximately ±0.5°C.

Figure 6 shows the experimental and model results of the nanofluid temperature as a function of time for a range of solar concentration ratios ($1 < C < 10$ suns, see Methods).

As the incoming solar light was absorbed by the nanofluid, the bulk fluid temperature began to rise due to sensible heating of the nanofluid. As the nanofluid temperature continued to increase, the evaporation rate and parasitic heat losses (*i.e.* natural convection and radiation) began to dominate the energy transfer mechanisms, until the steady state was reached (t > 2000 s) where all of the incoming solar energy was being converted to evaporation and parasitic heat losses.

The heat transfer model agrees well with the experimentally measured time-dependent temperature profile of the bulk nanofluid. This indicates that the fluid is directly heated *via* conduction by the absorbing nanoparticles at the surface and that vapor is not being generated at the nanoparticles themselves in a non-equilibrium fashion as described previously. If the vapor was indeed generated at the nanoparticle, and not the liquid-air interface, the bulk temperature profile would be reduced, due to the localized heat generation.

Our model becomes less accurate in steady-state operation (t > 2000 s) due to the changing concentration of nanoparticles as water leaves the system, especially near the liquid-air interface. The evaporation of water left a concentrated layer of hydrophobic GCB particles, which formed a skin at the interface, and restricted evaporation. This reduced the evaporation heat transfer coefficient below that of pure water (used in the model), and contributed to the increasing temperature of the bulk fluid.[67] Furthermore, the latent heat of vaporization of nanofluids has been shown to potentially be significantly higher than the aqueous constituent alone,[68] leading to more energy required to evaporate the liquid water, lower evaporation rates, and higher steady-state temperatures. Although the lumped capacitance nanofluid model developed here does well at predicting the experimental behavior during nanofluid vapor generation, it fails to give a mechanistic understanding of the energy conversion mechanisms at the nanoparticle scale, which must be reconciled with additional modeling in order to gain a better understanding of the heat generation physics.

6. Particle Heating Model

To study the nanoparticle-fluid temperature difference, we used a 3D numerical simulation (COMSOL) to model an array of nanoparticles distributed evenly in a fluid medium. For such periodic structures, we can focus on the heat transfer in one unit cell to understand the entire structure. The COMSOL model consists of a particle-in-a-box, a single heated nanoparticle in a fluid domain (Fig.7a). The following details were used to construct the model. The dimensions of the box were based on the average nanoparticle spacing in the nanofluid, which for a 0.5 wt% GCB nanofluid was calculated to be ≈3 μm for a nanoparticle radius of 250 nm. The boundaries of the fluid box were insulated, due to symmetry (Fig.7b). A boundary heat flux was placed at the nanoparticle surface, which simulated the absorption of solar energy. The nanoparticle was assumed to be spherical, isothermal, and surrounded by liquid water. Only transient heat conduction was considered at these small length scales. Non-equilibrium nanoscale heat conduction effects were not considered due to the relatively high interfacial conductance at carbon-water interfaces.[69,70]

At time scales on the order of a few seconds, the temperature variation across the fluid box was negligible, < 0.01 K. This is not surprising, as the spacing between nanoparticles in the fluid is very small (< 3 μm), and the corresponding Fourier number is high ($Fo > 10^4$). This further supports a global temperature rise in the fluid medium as the proposed mechanism of evaporation.[46] Only at very short time scales (~μs) and high solar intensities (~10^5 suns) can a temperature difference of 100K be found over the fluid box. This high solar concentration is roughly in agreement with the laser intensities required for nanobubble formation in previous studies, and is larger than achievable solar concentrations.[37,38,42]

To study the effect of overlapping thermal boundary layers of nearby nanoparticles on the bulk fluid temperature, the particle separation distance ($2L_{\text{fluid}}$) was varied. In previous works, models of a single nanoparticle in an infinite medium have been considered.[6,42] However, this ignores the heating effects of nearby nanoparticles in a real fluid and is only valid for short time scales where the individual heating profile has not reached the neighboring particles.[46,71] Fig.7c shows the fluid temperature profile as a function of normalized distance from the nanoparticle wall in the x-direction for different particle spacings (nanoparticle concentration) and a constant heating time of 2 μs. The results show that the 3μm box approaches the limit of the heated sphere in an infinite medium, and increasing the box size does not decrease the temperature profile of the liquid. Conversely, decreasing the fluid domain size to approach $L_{\text{fluid}} \approx 0.75$ μm resulted in significant thermal boundary overlap and fluid heating. The results show that the sustained heating of a large number of dispersed nanoparticles can produce a significant global fluid temperature rise.

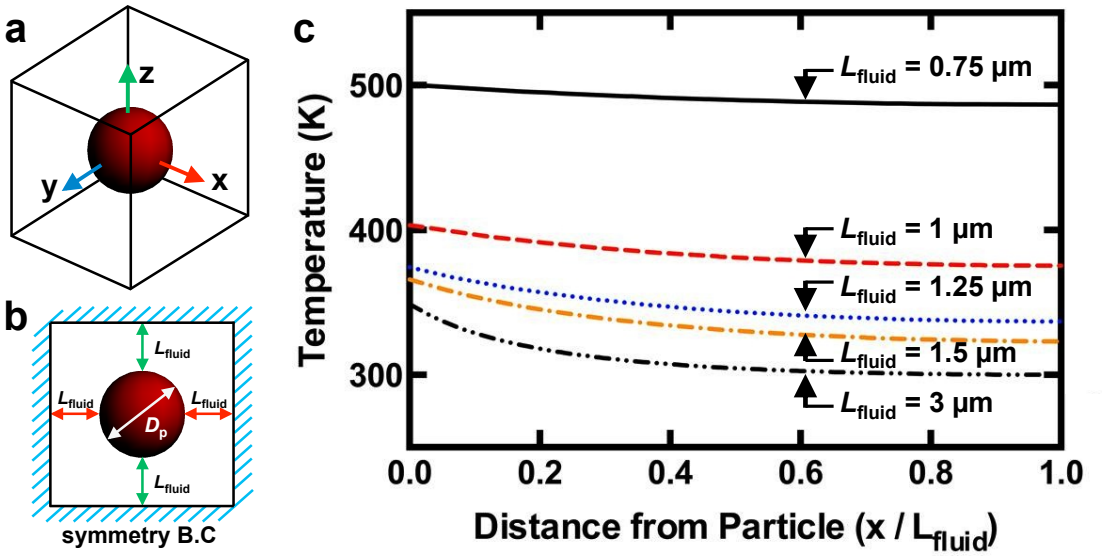

Figure 7. (a) Isometric view of the COMSOL model domain showing the heated nanoparticle (red sphere) in a fluid box surrounding it. (b) Side view of the fluid domain showing the critical simulation dimensions: particle diameter (D_p), and distance from the particle edge to the domain boundary (L_{fluid}). (c) Mean fluid temperature as a function of normalized distance from the nanoparticle wall for 5 different fluid domain sizes. As the fluid domain decreased in size, the fluid temperature increased due to the larger thermal boundary overlapping between particles.

A natural question is to compare using nanofluids versus surface absorbers for generating vapor. Our work has focused on evaporating water at temperatures below 100°C, and is expected to outperform (5-10%) a surface absorber designed for similar applications (see Supporting Information). Another related application is in solar boiling of water. Here, the nanofluid operates similarly to a surface absorber, since a tuned nanofluid will absorb sunlight at the surface for maximum heat concentration. A nanofluid-based absorber may have comparative advantages in high flux applications, due to its ability to increase critical heat flux[40,72]

In the future, it would be interesting to investigate methods to further increase the temperature of the generated vapor *via* vapor flow restriction. By confining the vapor escape from the nanofluid receiver, the evaporation heat transfer and overall heat transfer coefficient of the entire device decreases, increasing the temperature of the fluid within. In addition, the capability of directly generating steam at elevated pressures needs further investigation. Typically, in a power generation cycle, high temperature pressurized steam is required for efficient operation, with steam-based Rankine cycles using steam at temperatures in the range of 300-500°C. Currently, a more suitable power application for our small-scale device is the organic Rankine cycle, which requires working fluid temperatures of only 100-200°C.[73,74] Another potential area for future work is developing approaches for superheating the generated steam using solar energy to high temperatures for power generation applications. In applications requiring turbines,

condensing liquid from the working vapor causes erosion on the turbine blades, and increases costs.

Another area for future work is in integrating nanofluids into current cycle designs, such as a solar absorption cooling cycle. Depending on whether a system is closed-loop or open loop, the fluid influx can contain respectively nanoparticles or pure fresh water. In the closed-loop case such as an absorption refrigeration cycle, the nanoparticles are small enough to pass through pumps, and the various concentrations of fluids can be remixed. In an open-loop cycle, when operating at steady state, fresh water is required to feed the receiver and balance the water vapor leaving the system. This ensures a constant nanoparticle concentration. Possibly a mixing element will be needed to evenly disperse the nanoparticle, but pumps in a closed-cycle can accomplish this task. In general, agitation tends to decrease the aggregation of the system, as evidenced by the nanofluid preparation (ultrasonication bath for dispersing). This actually increases the effectiveness of the volumetric receiver, as shown in the Figure 3.

7. Conclusion

In summary, we demonstrated a high efficiency (69%) nanofluids-based solar receiver for direct vapor generation, using low concentration sunlight (10 suns). At such low solar concentrations, a nanofluid solar receiver may be used in lower cost systems that do not require the use of active sun-tracking devices, although monthly repositioning may be required. Three water-based nanofluids, graphitized carbon black, graphene, and carbon black, were tested in the receiver. We experimentally demonstrated and theoretically verified that in transient situations, such as in solar vapor generation, the graphitized carbon black and graphene nanofluids outperformed the carbon black nanofluid by 7%, after 1.5 hours of illumination. To show global fluid temperature rise as the more accurate vapor generation mechanism for nanofluids at the studies solar concentrations ($1 < C < 10$ suns), we constructed heat transfer models for the receiver at the device and nanoparticle scales. The device scale lumped capacitance model closely predicted the bulk temperature response of the nanoparticle receiver. The particle model showed that at feasible solar concentrations and illumination times, it is highly unlikely to achieve local temperature gradients leading to nanobubble generation around the nanoparticle, as proposed previously. This work demonstrates a solar vapor generation platform that promises to be low cost and scalable for a wide-range of solar-based applications such as power generation, distillation, and sterilization.

Acknowledgements

We thank K. McEnaney and D. Kraemer with help operating the solar simulator, and T. McClure and the Center for Materials Science and Engineering for the use of the UV-Vis Spectrophotometer. This work has implications in solar steam generation, and was partially supported by the Cooperative Agreement between the Masdar Institute of Science and Technology, UAE and the Massachusetts Institute of Technology (MIT), USA (for the steam generation). We gratefully acknowledge funding support from the MIT S3TEC Center, an Energy Frontier Research Center funded by the Department of Energy, Office of Science, Basic Energy Sciences under Award # DE-FG02-09ER46577 (for the experimental facility). Some of the existing infrastructure used in the research

was purchased under the S3TEC grant. This work was performed in part at the Center for Nanoscale Systems (CNS), a member of the National Nanotechnology Infrastructure Network (NNIN), which is supported by the National Science Foundation under NSF award no. ECS-0335765. CNS is part of Harvard University.

ASSOCIATED CONTENT

Supporting Information Available: Additional information is provided, including: 1) experimental details on the efficiency measurements, 2) details on the classical heat transfer model. Experimental details on the small cuvette measurement, 3) details of the COMSOL model for heat losses in the efficiency measurement, 4) additional SEM images of the nanoparticles, 5) bulk optical data for the nanofluids, 6) optical characterization of the nanoparticle agglomerate size, 7) details of the Mie theory calculation, and 8) details of the transient efficiency model. This material is available free of charge *via* the Internet at http://pubs.acs.org.

AUTHOR INFORMATION

Corresponding Author: Gang Chen, gchen2@mit.edu

Author Contributions: G. Ni, H. Ghasemi, N. Miljkovic, S.V. Boriskina, M. Rahman, T. Zhang and G. Chen conceived the idea. G. Ni, N. Miljkovic and H. Ghasemi conducted the experiments. N. Miljkovic, X.P. Huang and G. Ni did the theoretical modeling. Y. Xu and C.T. Lin synthesized the nanofluids. J.J. Wang and G. Ni performed the optical characterizations. G. Chen guided the work. G. Ni and N. Miljkovic wrote the paper. All authors commented on the paper and have given approval to the final version of the manuscript.

Conflict of Interest: The authors declare no competing financial interest.

References

[1] M.S. Bohn, K.Y. Wang, J. Sol. Energy Eng. 110 (1988) 45.
[2] B. Norton, (2014) 123.
[3] M. Thirugnanasambandam, S. Iniyan, R. Goic, Renewable Sustainable Energy Rev. 14 (2010) 312.
[4] G.T. Machinda, S.P. Chowdhury, S. Chowdhury, S. Kibaara, R. Arscott, in:, IEEE India Conference, IEEE, 1981, pp. 1–6.
[5] Y. Tian, C.Y. Zhao, Appl. Energy 104 (2013) 538.
[6] O. Neumann, A.S. Urban, J. Day, S. Lal, P. Nordlander, N.J. Halas, ACS Nano 7 (2013) 42.
[7] W.F. Bogaerts, C.M. Lampert, J. Mater. Sci. 18 (1983) 2847.
[8] Q.-C. Zhang, Sol. Energy Mater. Sol. Cells 62 (2000) 63.
[9] D. Mills, Sol. Energy 76 (2004) 19.
[10] C.E. Kennedy, 1617 (2002) 1.
[11] O.P. Agnihotri, B.K. Gupta, Solar Selective Surfaces, Wiley, New York, 1981.
[12] C.E. Kennedy, National Renewable Energy Laboratory (NREL), (2008) 1.
[13] O. Mahian, A. Kianifar, S.A. Kalogirou, I. Pop, S. Wongwises, Heat Mass

Transfer 57 (2013) 582.
[14] H. Price, E. Lüpfert, D. Kearney, E. Zarza, G. Cohen, R. Gee, R. Mahoney, J. Sol. Energy Eng. 124 (2002) 109.
[15] A. Veeraragavan, A. Lenert, B. Yilbas, S. Al-Dini, E.N. Wang, Heat Mass Transfer 55 (2012) 556.
[16] A. Lenert, Y.S.P. Zuniga, E.N. Wang, in:, 14th International Heat Transfer Conference, Washington DC, 2010, pp. 499–508.
[17] A. Lenert, E.N. Wang, Sol. Energy 86 (2012) 253.
[18] R.A. Taylor, P. Phelan, R. Adrian, A. Gunawan, T. Otanicar, in:, ASME 2011 5th International Conference on Energy Sustainability, American Society of Mechanical Engineers, Washington DC, 2011, pp. 1927–1936.
[19] A.O. Govorov, H.H. Richardson, Nano Today 2 (2007) 30.
[20] M.T. Carlson, A.J. Green, H.H. Richardson, Nano Lett. 12 (2012) 1534.
[21] A. Sanchot, G. Baffou, R. Marty, A. Arbouet, R. Quidant, C. Girard, E. Dujardin, ACS Nano 6 (2012) 3434.
[22] H. Tyagi, P. Phelan, R. Prasher, J. Sol. Energy Eng. 131 (2009) 041004.
[23] R.A. Taylor, P.E. Phelan, T.P. Otanicar, C.A. Walker, M. Nguyen, S. Trimble, R. Prasher, J. Renewable Sustainable Energy 3 (2011) 023104.
[24] N. Arai, Y. Itaya, M. Hasatani, Sol. Energy 32 (1984) 49.
[25] T. Fend, B. Hoffschmidt, R. Pitz-Paal, O. Reutter, P. Rietbrock, Energy 29 (2004) 823.
[26] N.E. Wijeysundera, V. Thevendran, Sol. Energy 40 (1988) 127.
[27] T. Fend, R. Pitz-Paal, O. Reutter, J. Bauer, B. Hoffschmidt, Sol. Energy Mater. Sol. Cells 84 (2004) 291.
[28] R. Pitz-Paal, B. Hoffschmidt, M. Böhmer, M. Becker, Sol. Energy 60 (1997) 135.
[29] F.L. Lansing, V. Clarke, R. Reynolds, Energy 4 (1979) 685.
[30] A.O. Govorov, W. Zhang, T. Skeini, H. Richardson, J. Lee, N.A. Kotov, Nanoscale Res. Lett. 1 (2006) 84.
[31] R. Bertocchi, J. Karni, A. Kribus, Energy 29 (2004) 687.
[32] D. Han, Z. Meng, D. Wu, C. Zhang, H. Zhu, Nanoscale Res. Lett. 6 (2012) 1.
[33] F. Miller, R. Koenigsdorff, Sol. Energy Mater. 24 (1991) 210.
[34] T.P. Otanicar, P.E. Phelan, R.S. Prasher, G. Rosengarten, R.A. Taylor, J. Renewable Sustainable Energy 2 (2010) 033102.
[35] S.V. Boriskina, H. Ghasemi, G. Chen, Mater. Today 16 (2013) 375.
[36] N.J. Hogan, A.S. Urban, C. Ayala-Orozco, A. Pimpinelli, Nano Lett. (2014).
[37] Z. Fang, Y.-R. Zhen, O. Neumann, A. Polman, F.J. García de Abajo, P. Nordlander, N.J. Halas, Nano Lett. 13 (2013) 1736.
[38] E. Lukianova-Hleb, Y. Hu, L. Latterini, L. Tarpani, S. Lee, R.A. Drezek, J.H. Hafner, D.O. Lapotko, ACS Nano 4 (2010) 2109.
[39] R. Saidur, T.C. Meng, Z. Said, M. Hasanuzzaman, A. Kamyar, Heat Mass Transfer 55 (2012) 5899.
[40] S.J. Kim, I.C. Bang, J. Buongiorno, L.W. Hu, International Journal of Heat and Mass Transfer 50 (2007) 4105.
[41] S.M. You, J.H. Kim, K.H. Kim, Appl. Phys. Lett. 83 (2003) 3374.
[42] J. Lombard, T. Biben, S. Merabia, Phys. Rev. Lett. 112 (2014) 105701.
[43] S. Baral, A.J. Green, M.Y. Livshits, A.O. Govorov, H.H. Richardson, ACS Nano

8 (2014) 1439.
[44] G. Baffou, J. Polleux, H. Rigneault, S. Monneret, J. Phys. Chem. C 118 (2014) 4890.
[45] V. Kotaidis, C. Dahmen, G. von Plessen, F. Springer, A. Plech, J. Chem. Phys. 124 (2006) 184702.
[46] P. Keblinski, D.G. Cahill, A. Bodapati, C.R. Sullivan, T.A. Taton, J. Appl. Phys. 100 (2006) 054305.
[47] M.J. Montes, A. Abánades, J.M. Martínez-Val, Sol. Energy 83 (2009) 679.
[48] B. Kelly, U. Hermann, M. Hale, in:, Proceedings of Solar Energy Forum: the Power to Choose, Washington DC, 2001, pp. 393–398.
[49] V. Quaschning, W. Ortmanns, in:, ISES Solar World Congress 2003, Goteborg, SE, 2003, pp. 14–19.
[50] G. Resch, T. Faber, R. Haas-EEG, M. Ragwitz, A. Held, I. Konstantinaviciute-LEI, Report (D4) of the IEE Project OPTRES: Assessment and Optimisation of Renewable Support Schemes in the European Electricity Market (2006) 35.
[51] J.J. O'Gallagher, Nonimaging Optics in Solar Energy, Synthesis Lectures on Energy and the Environment: Technology, Science, and Society, 2008.
[52] G.J. Kolb, C.K. Ho, T.R. Mancini, J.A. Gary, Power Tower Technology Roadmap and Cost Reduction Plan, Sandia National Lab, 2011.
[53] O. Neumann, C. Feronti, A.D. Neumann, A. Dong, K. Schell, B. Lu, E. Kim, M. Quinn, S. Thompson, N. Grady, Proc. Natl. Acad. Sci. U. S. a. 110 (2013) 11677.
[54] C.-Y. Su, A.-Y. Lu, Y. Xu, F.-R. Chen, A.N. Khlobystov, L.-J. Li, ACS Nano 5 (2011) 2332.
[55] V. Trisaksri, S. Wongwises, Renewable Sustainable Energy Rev. 11 (2007) 512.
[56] J. Buongiorno, D.C. Venerus, N. Prabhat, T. McKrell, J. Townsend, R. Christianson, Y.V. Tolmachev, P. Keblinski, L.-W. Hu, J.L. Alvarado, I.C. Bang, S.W. Bishnoi, M. Bonetti, F. Botz, A. Cecere, Y. Chang, G. Chen, H. Chen, S.J. Chung, M.K. Chyu, S.K. Das, R. Di Paola, Y. Ding, F. Dubois, G. Dzido, J. Eapen, W. Escher, D. Funfschilling, Q. Galand, J. Gao, P.E. Gharagozloo, K.E. Goodson, J.G. Gutierrez, H. Hong, M. Horton, K.S. Hwang, C.S. Iorio, S.P. Jang, A.B. Jarzebski, Y. Jiang, L. Jin, S. Kabelac, A. Kamath, M.A. Kedzierski, L.G. Kieng, C. Kim, J.-H. Kim, S. Kim, S.H. Lee, K.C. Leong, I. Manna, B. Michel, R. Ni, H.E. Patel, J. Philip, D. Poulikakos, C. Reynaud, R. Savino, P.K. Singh, P. Song, T. Sundararajan, E. Timofeeva, T. Tritcak, A.N. Turanov, S. Van Vaerenbergh, D. Wen, S. Witharana, C. Yang, W.-H. Yeh, X.-Z. Zhao, S.-Q. Zhou, J. Appl. Phys. 106 (2009) 094312.
[57] W.T. Xie, Y.J. Dai, R.Z. Wang, K. Sumathy, Renewable Sustainable Energy Rev. 15 (2011) 2588.
[58] R.A. Taylor, P.E. Phelan, T.P. Otanicar, R. Adrian, R. Prasher, Nanoscale Res. Lett. 6 (2011) 1.
[59] W. Yu, H. Xie, J. Nanomater. 2012 (2012) 1.
[60] L. Fedele, L. Colla, S. Bobbo, S. Barison, F. Agresti, Nanoscale Res. Lett. 6 (2011) 1.
[61] Y. Hwang, J.-K. Lee, J.-K. Lee, Y.-M. Jeong, S.-I. Cheong, Y.-C. Ahn, S.H. Kim, Powder Technol. 186 (2008) 145.
[62] M. Mehrali, E. Sadeghinezhad, S.T. Latibari, S.N. Kazi, M. Mehrali, M.N.B.M.

Zubir, H.S.C. Metselaar, Nanoscale Res. Lett. 9 (2014) 1.
[63] M.F. Modest, Radiative Heat Transfer, Academic Press, 1993.
[64] B.J. Stagg, T.T. Charalampopoulos, Combust. Flame 94 (1993) 381.
[65] T.L. Bergman, A.S. Levine, F.P. Incropera, D.P. Dewitt, Fundamentals of Heat and Mass Transfer, 7 ed., John Wiley & Sons, 2011.
[66] D.M. Kerslake, The Stress of Hot Environments, Reissue, Cambridge University Press, 2011.
[67] R.-H. Chen, T.X. Phuoc, D. Martello, Heat Mass Transfer 53 (2010) 3677.
[68] S. Lee, P.E. Phelan, L. Dai, R. Prasher, A. Gunawan, R.A. Taylor, Appl. Phys. Lett. 104 (2014) 151908.
[69] S.T. Huxtable, D.G. Cahill, S. Shenogin, L. Xue, R. Ozisik, P. Barone, M. Usrey, M.S. Strano, G. Siddons, M. Shim, P. Keblinski, Nat. Mater. 2 (2003) 731.
[70] P. Keblinski, J.A. Eastman, D.G. Cahill, Mater. Today 8 (2005) 36.
[71] G. Baffou, P. Berto, E. Bermúdez Ureña, R. Quidant, S. Monneret, J. Polleux, H. Rigneault, ACS Nano 7 (2013) 6478.
[72] H. Kim, Nanoscale Res. Lett. 6 (2011) 415.
[73] S. Quoilin, M. Orosz, H. Hemond, V. Lemort, Sol. Energy 85 (2011) 955.
[74] A.N.M. Delgado-Torres, L. García-Rodríguez, Energy Convers. Manage. 51 (2010) 2846.

TOC Graphic

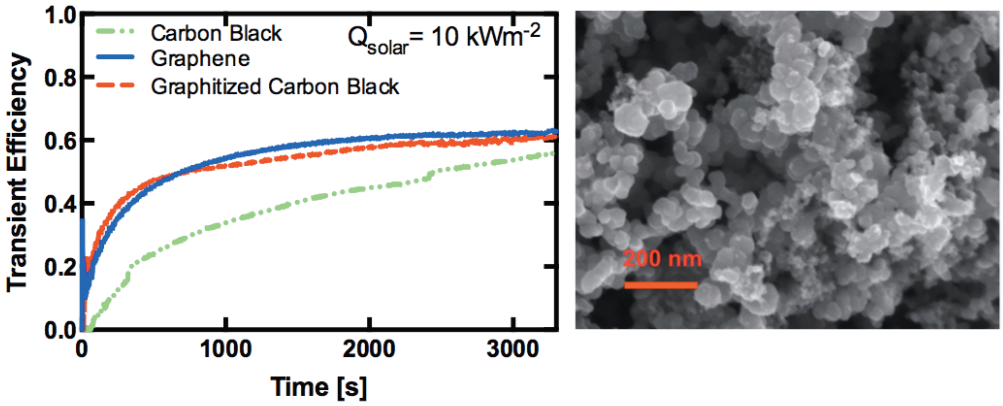
Carbon Black
Graphene
Graphitized Carbon Black
Q_{solar}= 10 kWm^{-2}
Transient Efficiency
1.0
0.8
0.6
0.4
0.2
0.0
0
1000
2000
3000
Time [s]
200 nm

Supplemental Information

Volumetric Solar Heating of Nanofluids for Direct Vapor Generation

George Ni[1], Nenad Miljkovic[1,2], Hadi Ghasemi[1,3], Xiaopeng Huang[1], Svetlana V. Boriskina[1], Cheng-Te Lin[1,4], Jian Jian Wang[1], Yanfei Xu[1], Md. Mahfuzur Rahman[5], TieJun Zhang[5], and Gang Chen[1,*]

[1]*Department of Mechanical Engineering, Massachusetts Institute of Technology, 77 Massachusetts Ave, Cambridge, Massachusetts 02139*

[2]*Department of Mechanical Science and Engineering, University of Illinois, Urbana, Illinois, 61801, USA*

[3]*Department of Mechanical Engineering, University of Houston, Houston, Texas, 77204, USA*

[4]*Key Laboratory of Marine New Materials and Related Technology, Zhejiang Key Laboratory of Marine Materials and Protection Technology, Ningbo Institute of Material Technology & Engineering, Chinese Academy of Sciences, Ningbo, 315201, China*

[5]*Department of Mechanical and Materials Engineering, Masdar Institute, Masdar City, Abu Dhabi, United Arab Emirates*

* Address correspondence to: gchen2@mit.edu

S1. Efficiency Measurement Setup

The vapor generation efficiency measurements were carried out using the set up shown in Figure S1. A solar simulator (ScienceTech, SS-1.6K) generated solar light that was reflected downwards using a mirror (Alanod, Miro Reflective 90), and passed through a Fresnel lens (Edmund Optics, polymer 6-inch focal length). The solar radiation then passed through an aperture (polished copper, 25.1mm diameter), resulting in nearly all light being incident on the nanofluid. The solar simulator conforms to class A standards, according to ASTM E927-10. The mirror was +85% specularly reflective, with a total reflectance of +90%. The nanofluid was housed in a custom built container made of acrylic and aerogel pieces to limit parasitic side losses. The total weight of the container is less than 170g.

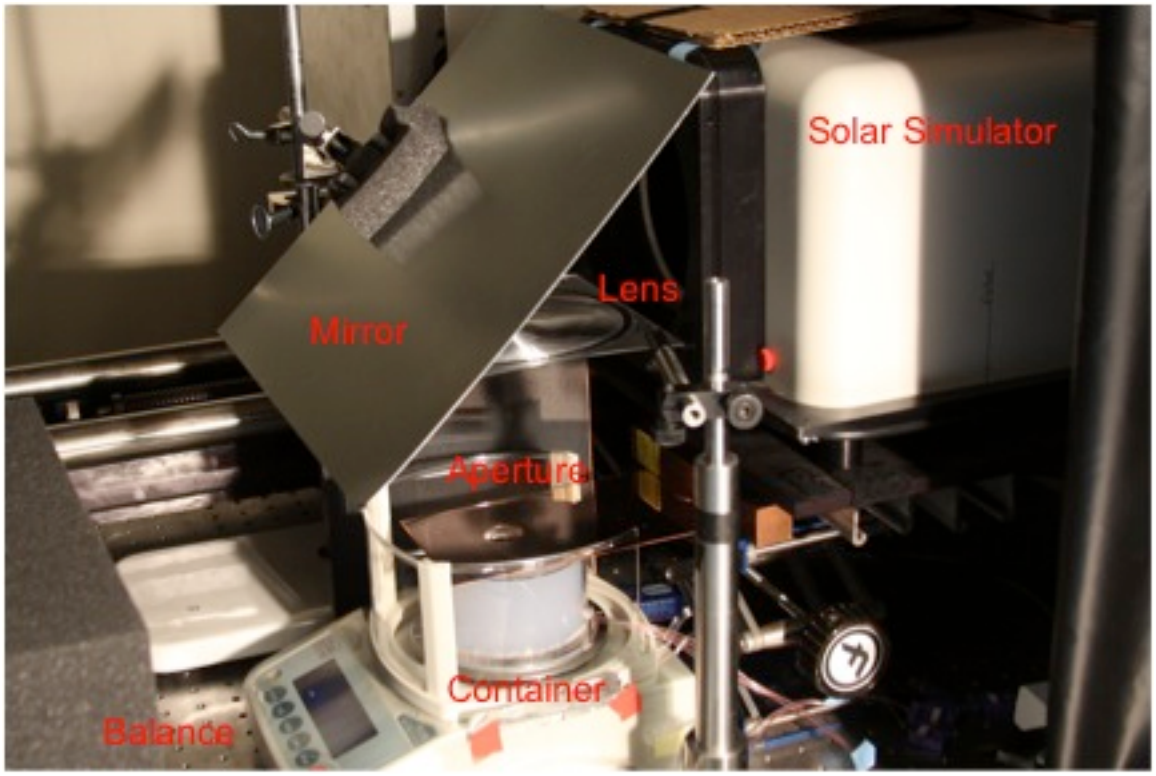

Figure S1: Efficiency testing setup for nanofluids-based solar receiver.

The nanofluid container is constructed out of two concentric acrylic tubes, with a layer of aerogel particles (Cabot, Lumira Aerogel Particles) in between to serve as an insulator to minimize radial heat losses. The aerogel particles are sealed from the environment with acrylic discs. The nanofluid is exposed to the ambient, to allow vapor escape. Four E-type thermocouples were inserted into the nanofluid container to measure the fluid temperature at different distances from the nanofluid-air interface. As the nanofluid evaporated, the fluid level dropped below each thermocouple, allowing measurement of the liquid/vapor interface. The mass loss was measured using balance (A&D, FX300i) with a resolution of 1mg, and calibrated up to 300g.

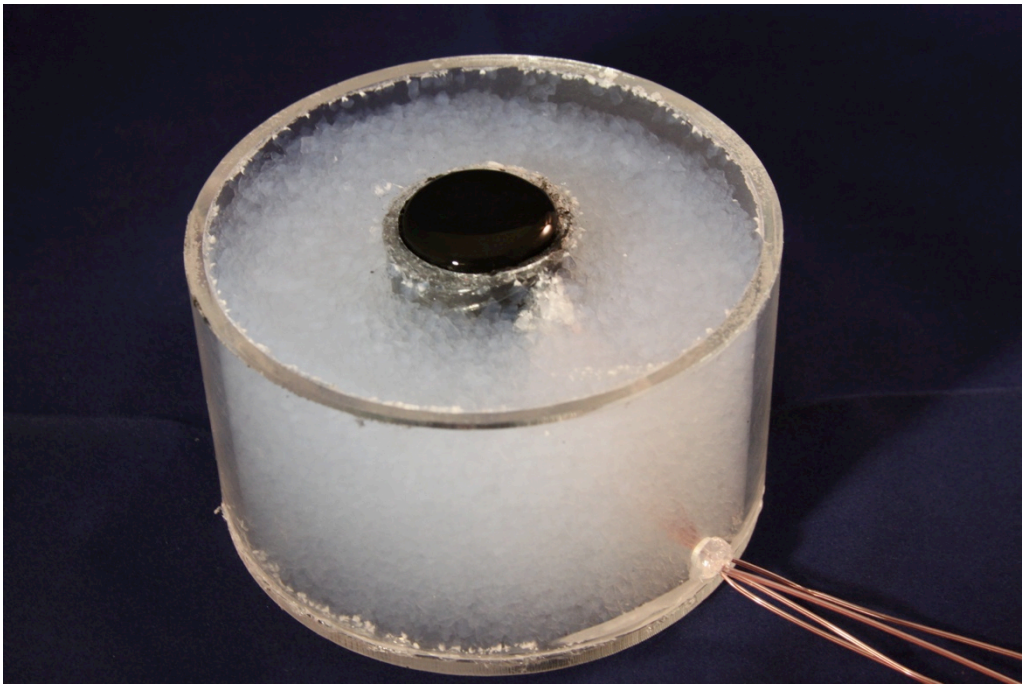

Figure S2: Close up picture of the nanofluids-based solar receiver.

The total incoming power at the nanofluid surface was measured using a thermopile (Newport, 818P-040-55, 40W, 55 mm diameter) and power meter (1918-c), and is around 5W. The copper aperture is placed in a fixed location, and not touched during the entire experiment. To capture all the solar radiation passing through the aperture, the thermopile is placed underneath, as close to the aperture as possible. Prior to the experiment, the power was measured at several times over a 10-minute interval, and the power fluctuation was less than 1%. The thermopile is then removed, the aperture covered with a metal foil, and the nanofluids container is placed underneath. The nanofluid container is briefly aligned to capture as much light as possible, and then the temperature is stabilized to ~25°C before the experiment begins. The mass is measured over a 10-minute period to ensure no drifting occurs, other than ambient evaporation of the nanofluid.

SEM images of the three different nanofluids were taken, and are shown in Section S4. The graphitized carbon black and carbon black look remarkably similar. In contrast, their transient efficiency are the best and worst out of the nanofluids tested, respectively. This indicates the importance of surface effects on the performance of nanofluid evaporation.

S2. Heat Transfer Model

A different experimental setup is used to compare with the heat transfer model, and is shown in Figure S3. This setup consists of direct illumination from the solar simulator (ScienceTech SS-1.6K) to a polymer cuvette holding 3mL of nanofluid. Water is allowed to evaporate to the ambient from the top. To measure the bulk liquid temperature, four E-type thermocouples are placed in the cuvette, entering the sides at different heights. The data is acquired using a DAQ board (NI USB-6210 with cold-

junction compensation). A power meter (1918-c) and thermopile (Newport, 818P-040-55, 40W, 55 mm diameter) are used to measure the incoming solar radiation. Experiments are run for over one hour, and solar concentrations of 1, 3, 5, 7, and 10 suns are used.

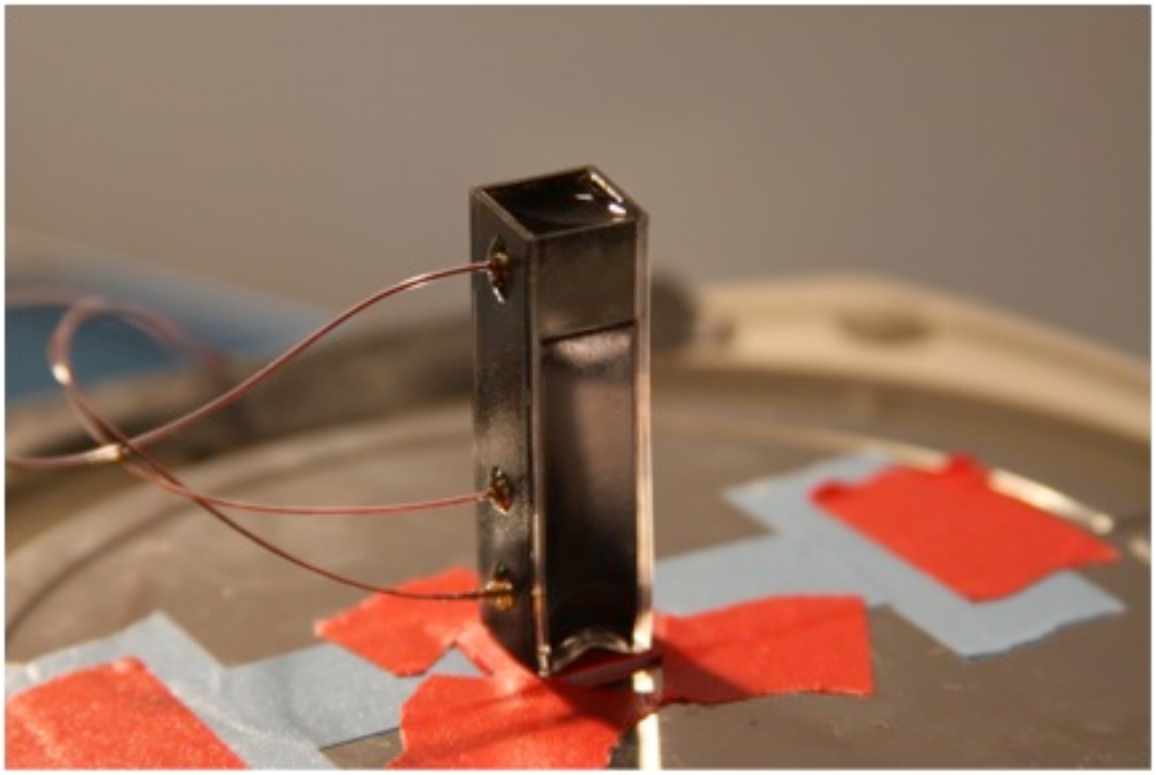

Figure S3: Cuvette nanofluids receiver built to compare with the classical heat transfer model.

To simplify the model, the following assumptions were made. All incoming radiation was absorbed in the nanofluid, and all surfaces emit blackbody radiation to the ambient temperature of 25°C. The fluid is isothermal, and the Biot number of 0.02 confirms this. This assumption is further confirmed by the thermocouples in the bulk fluid, where a maximum temperature difference of 4°C was measured. Average heat transfer coefficients are valid over all nanofluid and cuvette surfaces. The thermal resistances in the walls of the cuvette are negligible. A discrete simulation was used to model the transient temperature profile of the heat transfer equation.

To model the cuvette experiments, three heat transfer coefficients were used. The heat transfer values below are given for the case of the 1 sun experiment, with the steady state temperature used to determine the relevant dimension numbers. The Nusselt number for natural convection off a vertical plate[1] was

$$\overline{Nu_L} = 0.68 + \frac{0.387 Ra_L^{1/6}}{[1+(\frac{0.492}{\mathrm{Pr}})^{9/16}]^{4/9}} \qquad \text{(S.1)}$$

and the heat transfer coefficient was 5.58 W/m^{2}K. For natural convection leaving the evaporating surface[1], the correlation was

$$\overline{Nu_L} = 0.54 Ra_L^{1/4} \quad \text{(S.2)}$$

with a heat heat transfer coefficient of 13.44 W/m^{2}K. Pr is the Prandtl number, Ra the Rayleigh number, and Nu the Nusselt number. The evaporation heat transfer coefficient is 16.5x the natural convection coefficient[2], and was 221.8 W/m^{2}K.

The governing heat equation used is an energy balance accounting for the incoming solar radiation, the outgoing radiation emissions, natural convective losses, and the evaporation of the fluid. The fluid is treated as a lumped capacitance body.

S3. COMSOL Model

A COMSOL model was constructed to simulate the heat flows through the nanofluids container. The actual experiment involved a constantly lowering evaporation surface from the nanofluid, because water was continually leaving the system. To simplify the model, only a static heat transfer model was considered. To ensure model fidelity to the experiment, four boundary conditions were imposed: 1) evaporation efficiency, 2) incoming solar radiation, 3) evaporation surface temperature, 4) and temperature of the underlying bulk nanofluid at a specified depth. With these constraints matched, the temperature distribution in the COMSOL model matches the experimental conditions.

The following parameters were used in the COMSOL model. A natural convection heat transfer coefficient of 7 W/m^{2}K was used on all exterior surfaces of the model, as well as the evaporation surface. All surfaces had a surface emissivity of 1 for radiation losses to an ambient temperature of 25°C. The bottom of the container is insulated, due to low thermal contact with the environment. A solar flux of 10kWm^{-2} was incident on the evaporating surface. The evaporation heat transfer coefficient of the evaporating surface was fit to satisfy the aforementioned four boundary conditions. Three materials were used in the container: 1) water, to simulate the nanofluids, 2) aerogels with thermal conductivity 0.02 W/m^{2}K, specific heat 10 J/kgK, and density 100 kg/m^3, and 3) acrylic with thermal conductivity 0.18 W/m^{2}K, specific heat 1470 J/kgK, and density 1180 kg/m^3.

A temporal study was used to include the effect of heat storage in the temperature distributions. The time used (3000 s) to analyze the losses corresponds roughly to the time used to determine the four boundary conditions. The results of the COMSOL model are shown in Figure S4.

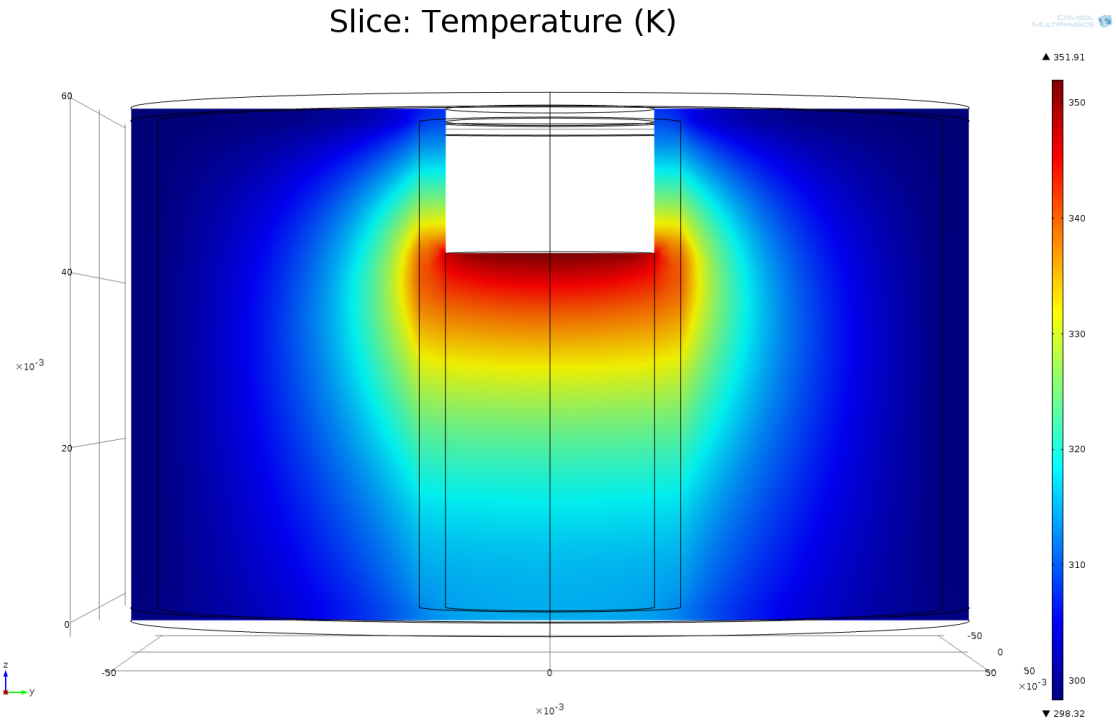

Figure S4: COMSOL model of the nanofluids-based solar receiver.

The four boundary conditions are closely matched with the COMSOL model, and the fitted evaporation rate corresponds to the evaporation measured in the experiment (69%). The radiation losses and convection losses from the evaporation surface are 4% and 3%, respectively. In a 1 cm slice of nanofluid directly underneath the evaporation surface, 9% is conducted radially into the container, and 9% are conducted axially into the nanofluid below. Only 12% is convected away from the outer surfaces of the container, which indicates the container is still being heated.

S4. SEM Images

SEM images were taken of the three nanofluids to show their morphology. The morphology of GCB and CB are quite similar, despite the drastic difference in dynamic performance. The graphene nanoflakes are sheet like, as expected.

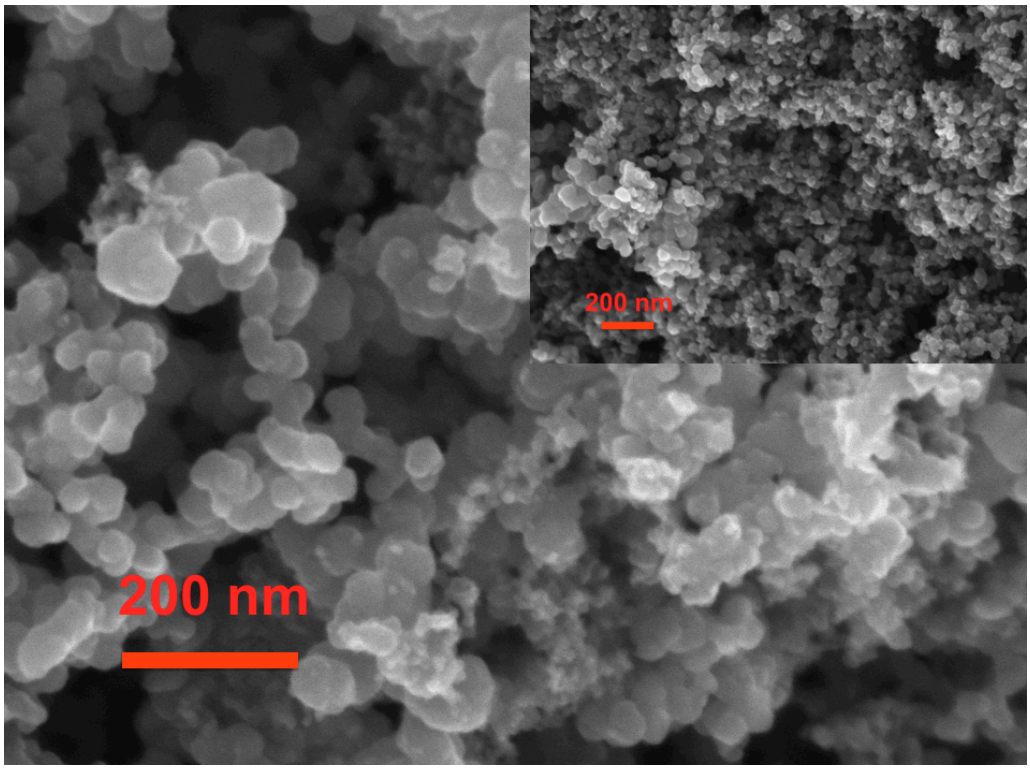

Figure S5: Carbon Black SEM image

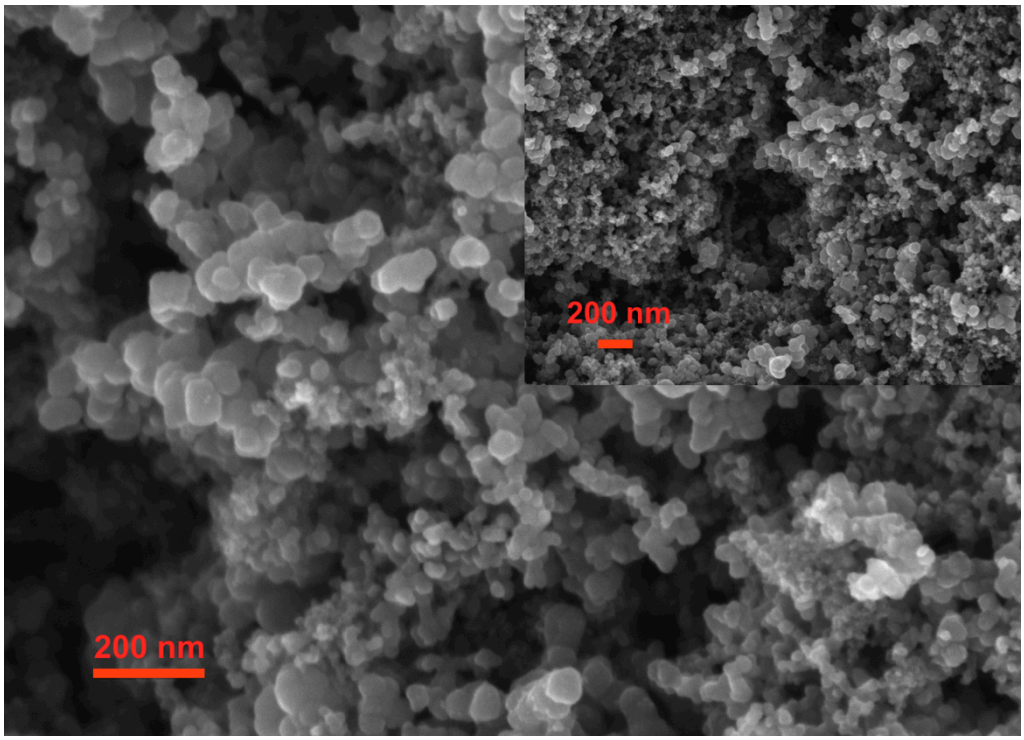

Figure S6: Graphitized Carbon Black SEM image

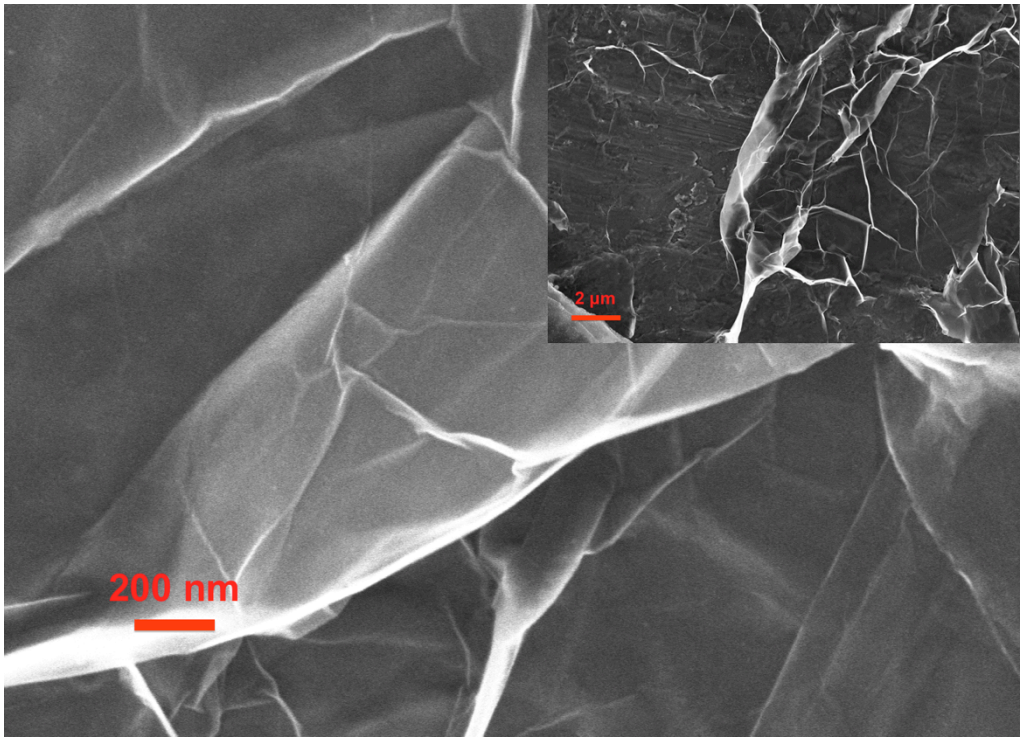

Figure S7: Graphene flakes exfoliated from graphite using an electrochemical method.[3]

S5. Optical Properties

Specular reflectivity and direct-direct transmission data were taken for the nanofluids in the optical range of 350nm-1900nm, and is shown in Figure S8. A holder was constructed out of two microslide glasses with smooth surfaces to contain the nanofluids for the reflectivity measurement, which was made on a Cary 500i UV-Vis-NIR Dual-Beam Spectrophotometer. The microslide reflectivity were individually measured, and subtracted from the measurement with glass.

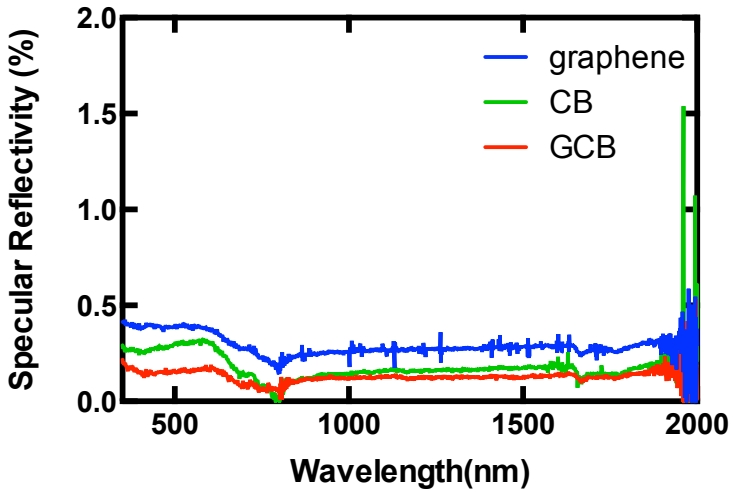

Figure S8: Specular reflectivity of GCB, graphene, and CB nanofluids.

A cuvette (Plastibrand, PMMA) was used in the transmission measurements. Transmission was below the detection limits of the UV-Vis spectrophotometer, across the entire spectrum.

S6. Nanofluid Agglomerate Sizes

To estimate the extinction coefficient, the average nanoparticle agglomerate size was measured. The extinction coefficient could not be directly determined via transmission measurements, due to the strongly absorbing properties in the nanofluid. From the nanoparticle agglomerate size, and the volume fraction of nanoparticles, the minimum extinction coefficient can be estimated.

To measure the particle size of GCB, a dynamic light scattering (DLS) measurement (DynaPro NanoStar, Wyatt Technology Corporation) was performed. Peaks of 20nm and 120nm were seen, with 96% of the mass in the 120nm peak. The polydispersity was ~22%. These results indicate the average agglomerate size of the GCB fluid to be 120nm, with some free particles of 20nm. The 20nm peak corresponds with the particle sizes in the SEM images shown in Section 4 of the Supplementary Information.

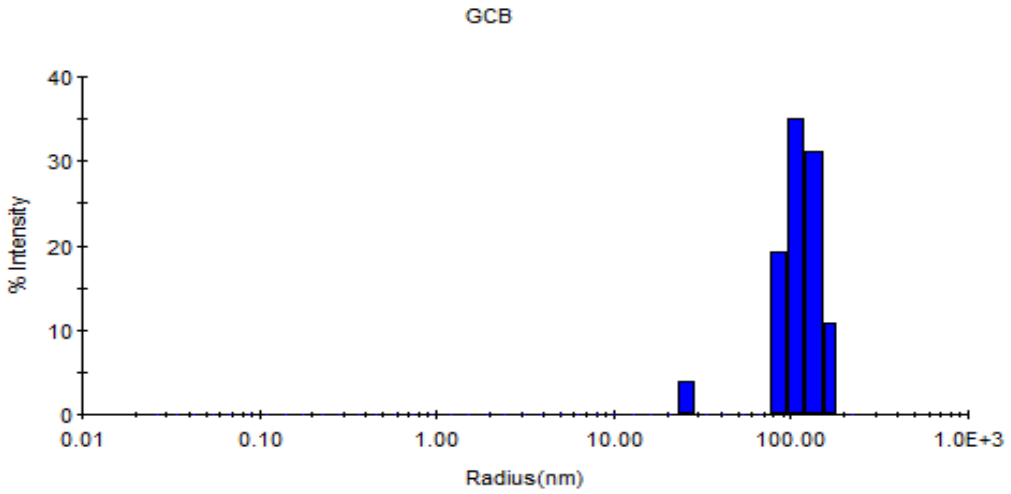

Figure S9: Results from a dynamic light scattering measurement of the GCB nanofluid

For determining the CB nanofluid agglomerate size, the dynamic light scattering measurement is not suitable, as the particle sizes were thought to be much larger. The DLS measurement was tried, but suitable data to match the light scattering model could not be obtained. Instead, the particle size was observed optically using an optical microscope. Figure S10 below shows the agglomeration structure of the CB nanofluid. The particles form large agglomerates, with diameter on the order of 1-50μm. For the purposes of our extinction coefficient estimation, we can start with a particle diameter of 5μm.

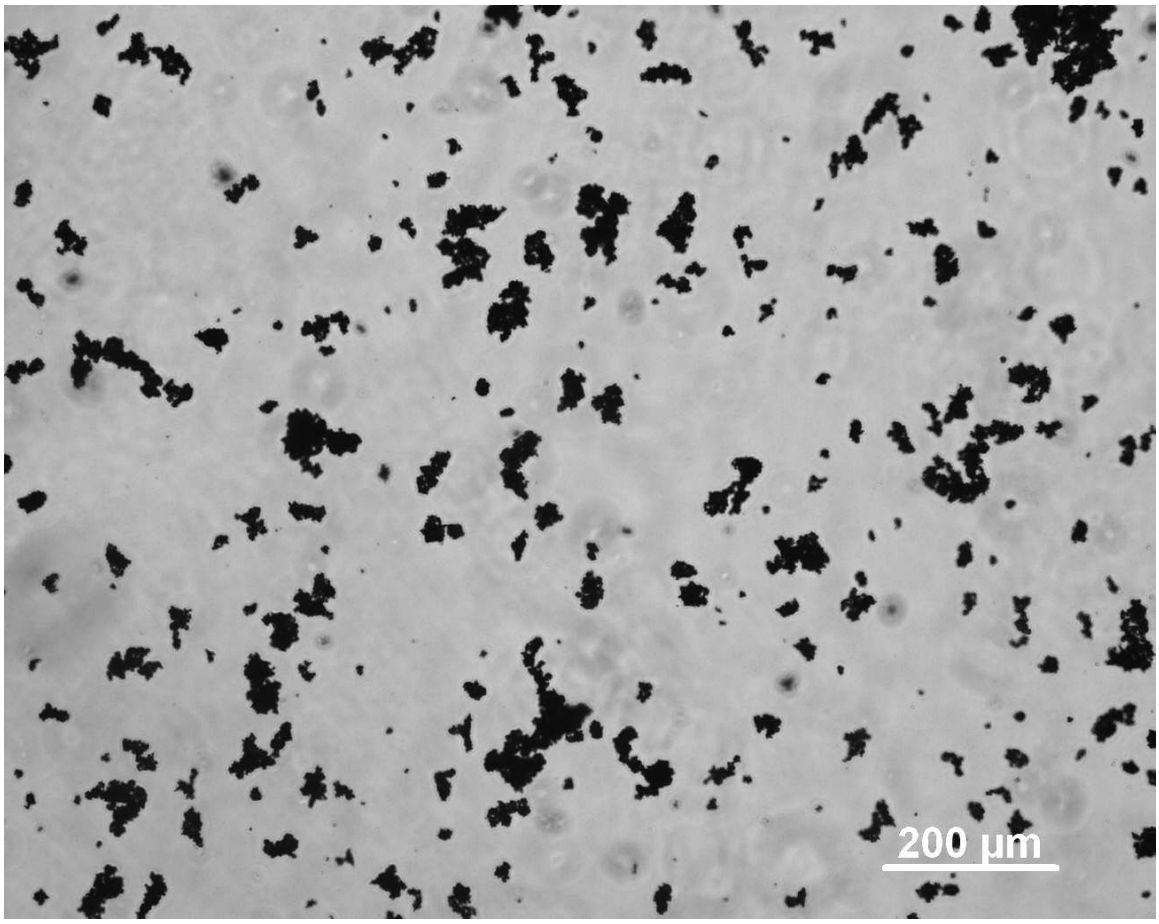

Figure S10: Optical image of the CB nanofluid. There is extensive agglomeration.

S7. Nanofluid Absorption Calculation

The extinction coefficient can be calculated from the agglomerate size, using Lorenz-Mie theory for a single spherical particle in the independent scattering regime. We approximated the particle radius in Mie theory as the agglomerate radius in the previously mentioned optical measurements (GCB: 110 nm, CB: 2.5µm). The index of refraction is determined from literature, and the bulk values are assumed valid for the agglomerate.[4] The size of the box surrounding the particle was calculated using the volume fraction of the nanoparticles in the nanofluid. It can be seen that the agglomerate cross section grows with r^2, whereas the agglomerate volume grows with r^3. Intuitively, in the absence of strong resonant scattering effects, the larger particle should have a smaller absorption coefficient.

The efficiency factor Q can was used to calculate the extinction coefficient using the following expressions,

$$\beta_{ext} = NQ_{ext}\pi r^2$$

$$\kappa_{abs} = NQ_{abs}\pi r^2 \quad \text{(S.3)}$$

$$\sigma_{sca} = NQ_{sca}\pi r^2$$

where N is the particle density, $Q_{ext}, Q_{abs}, Q_{sca}$ are the extinction, absorption, and scattering efficiencies. For the GCB, the interparticle spacing is 1.3 μm, and 30 μm for CB. In the studied nanofluids, the scattering and absorption cross sections are of similar magnitudes, and so a full equation of radiative transfer should be considered for an accurate determination of the heat generation in the nanofluid.[5] As an approximation, we use the extinction coefficient in Beer's law to model the heat generation within the nanofluid. This approximation underestimates the transient efficiency difference. Figure S11shows the results of the Lorenz-Mie theory calculation for the scattering directions. In the case of the CB agglomerate, most of the scattered light is forward directed, and so the absorption coefficient would give a more accurate estimate of the heat generation locations. However, this would also overestimate the difference in transient efficiency. Using our transient efficiency model (see Section S8) we determined the sensitivity of transient efficiency to extinction coefficient. If our calculated extinction coefficients are overestimated, the sensitivity plot shows that the GCB transient efficiency is relatively unaffected, where as the CB transient efficiency rises quickly with extinction coefficient.

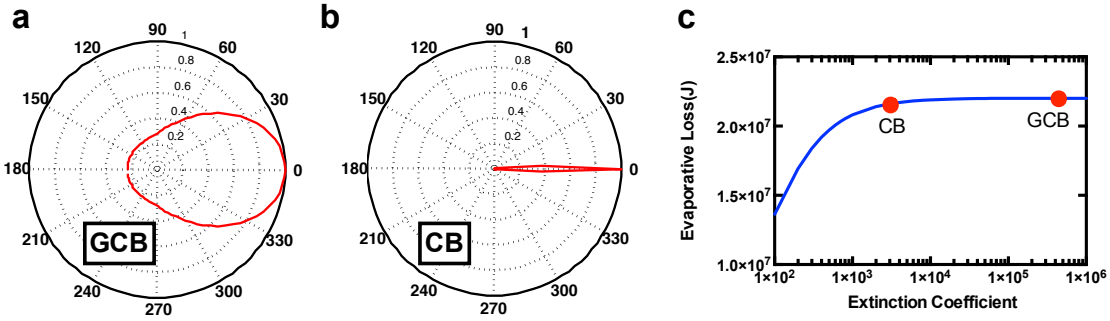

Figure S11: Normalized scattering phase functions for a)GCB and b)CB agglomerates using Mie theory. c) shows the sensitivity of transient efficiency to extinction coefficient.

Our calculations showed the GCB to have an extinction coefficient of 5.6×10^5 m^{-1}, and the CB to have an extinction coefficient of 1.6×10^3 m^{-1}. From this analysis, we can see that the extinction coefficient varied significantly, more than two orders of magnitude.

S8. Transient Efficiency Model

The variation in extinction coefficient affected the temperature of the nanofluid evaporation surface, especially in transient conditions. The nanofluid surface temperature affected the evaporative flux and the vapor generation efficiency of the device. This effect was particularly strong in transient conditions. For longer absorption depths, the heat generated must diffuse further before reaching the surface. To check the effect of the nanofluid extinction coefficient on the surface temperature, a simple 1D model was constructed which simulated the absorption characteristics of the nanofluid, as well as the heat losses in the system.

The heat transfer model was based on the time-dependent Fourier's law, with an exponential heat generation term that follows Beer's law for light absorption. The governing equation, and boundary and initial conditions are shown below.

$$\frac{\partial \Theta(x,t)}{\partial t} = \alpha_x \frac{\partial^2 \Theta(x,t)}{\partial x^2} + \frac{q_0 \lambda e^{-\lambda x}}{\rho c_p}$$

$$\Theta(H,t) = 0$$

$$-k_x \frac{\partial \Theta(0,t)}{\partial x} + h\Theta(0,t) = 0$$

$$\Theta(x,0) = 0$$

$\theta(x,t)$ is the temperature difference from ambient, x is the position along the nanofluids receiver, t is the time after illumination, H is the length of the nanofluids receiver, A_c is the cross sectional area for absorption, λ is the extinction coefficient, k is the nanofluid thermal conductivity, h is the evaporation heat transfer coefficient, α is the thermal diffusivity, ρ is the density of the fluid, c_p is the specific heat, and q_0 is the incident solar flux on the receiver. The boundary conditions of the model were a convective term on one side, which represented evaporation, and a temperature boundary condition on the other side. At initial conditions, the entire model was at ambient temperature. Heat is generated closer to the convective side of the model. The model was solved using the Green's functions method. The full transient and steady-state solution is shown in the Supporting information. The results are simulated using MATLAB, and the effect of extinction coefficient on surface heat flux compared.

$$\Theta(x,t) = \frac{q_0}{k\lambda}\left[-e^{-\lambda x} + \frac{e^{-H\lambda}\left(1 + \frac{hH}{k}\frac{x}{H}\right)}{1 + \frac{hH}{k}} + \frac{\left(H\lambda + \frac{hH}{k}\right)}{\left(1 + \frac{hH}{k}\right)}\left(1 - \frac{x}{H}\right)\right] - \frac{2q_0\lambda H^2}{k}\sum_{m=1}^{\infty} \frac{(\beta_m H)^2 + \left(\frac{hH}{k}\right)^2}{\left((\beta_m H)^2 + \left(\frac{hH}{k}\right)^2\right) + \frac{hH}{k}} \frac{\left(H\lambda + \frac{hH}{k}\right)\sin(\beta_m H) + e^{-H\lambda}\beta_m H}{(H\lambda)^2 + (\beta_m H)^2} \sin[\beta_m (H - x)] \frac{e^{-(\beta_m H)^2 \frac{\alpha t}{H^2}}}{(\beta_m H)^2}$$

$\theta(x,t)$ is the temperature difference from ambient, x is the position along the nanofluids receiver, t is the time after illumination, L is the length of the nanofluids receiver, A_c is the cross sectional area for absorption, λ is the extinction coefficient, k is the nanofluid thermal conductivity, h is the evaporation heat transfer coefficient, α is the thermal diffusivity, and β_m is the eigenvalue.

S9. Varying Weight Fraction of Nanoparticles

The previous sections described how the different nanoparticles created varying extinction coefficients in the nanofluids, due to the different agglomeration

characteristics. Another way to test the effect of extinction coefficient on transient efficiency is to keep the nanoparticle constant, but vary the weight fraction to get varying extinction coefficients. We conducted a comparison by measuring the transient efficiency of a GCB-based nanofluid with lower weight fraction (0.005 wt%), which created a fluid with a calculated extinction coefficient of 5.6×10^3 m^{-1}. We compared this fluid with the previous measurements of GCB (5.6×10^5 m^{-1}) and CB (1.6×10^3 m^{-1}), and found that the diluted GCB did indeed have a transient performance in between the GCB and CB. The results are shown in Figure S12. This confirms our hypothesis that the extinction coefficient of a nanofluid can have a strong effect on the transient efficiency in vapor generation.

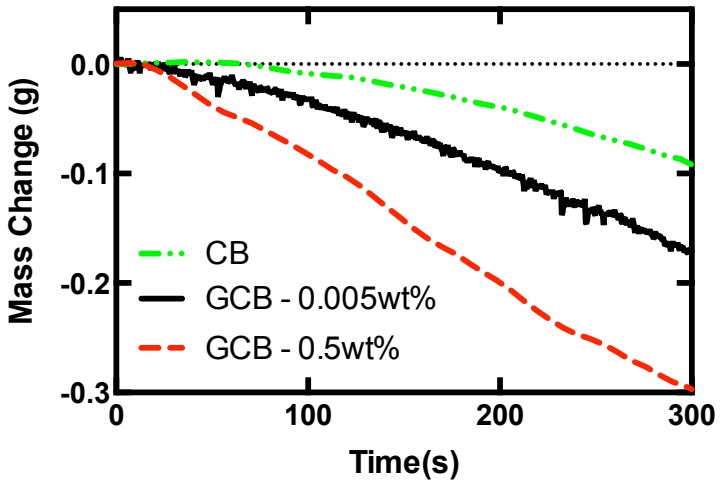

Figure S12: Comparing the transient efficiency of GCB nanofluids with varying nanoparticle concentrations to show the dependence on extinction coefficient.

S10. Comparison with a Surface Absorber

A direct comparison between nanofluid and surface absorbers is difficult, as each approach operates best at different regimes. To attempt an analysis for evaporation efficiency, we must make an assumption about the configuration of the surface absorber (Figure S13).

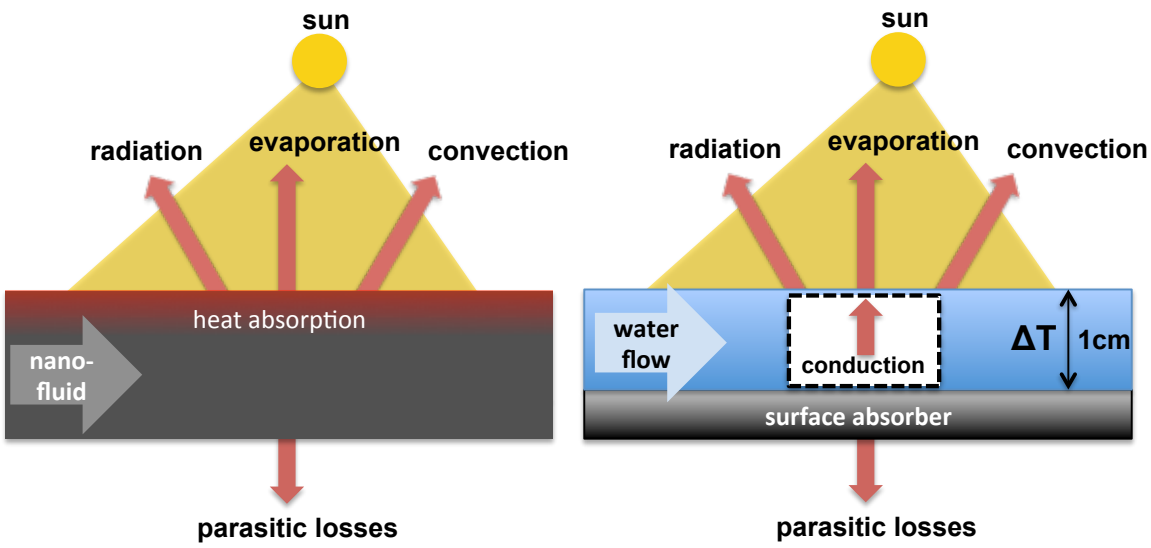

Figure S13: Nanofluid and surface absorber based solar evaporation configurations.

In the surface absorber, solar absorption occurs farther from the evaporation surface (~cm), compared to the nanofluid absorber (~ μ m). The larger separation in Figure S13 results in additional resistance from absorber to evaporation, and heat is forced towards other pathways (parasitic losses).

The following assumptions were made in this simple calculation: Conduction is assumed to dominate in the thin water layer. The evaporation heat transfer coefficients were determined experimentally in our lab (below), from a previous work.[6] Water is assumed to behave as a blackbody, based on its high optical loss constants in the infrared.[7] Given the thickness of the water layer (1cm) and the optical absorption coefficient of water (10^4-10^5 m^{-1}), it is unlikely for the emittance to be lower than 0.98, with the imperfection emittance due to some IR reflection. The convection heat transfer coefficient above the water is assumed 8 W/m^2K. The combined parasitic losses is determined from the nanofluid received experiments to be ~31 W/m^2K, and is assumed to be identical in the surface absorber case.

In this specific comparison, the nanofluid absorber can produce lower temperature vapor at efficiencies 5-10% higher (Figure S14). At higher temperatures, the surface absorber will start to boil at the surface-water interface, and a different comparison is warranted. Briefly, in the case of generating 100°C steam via boiling, the nanofluid absorber is expected to perform similarly to the surface absorber, since both can generate phase change near the solar absorption location. However, a nanofluid absorber can have versatile and simple geometries, such as in applications for developing countries.[8]

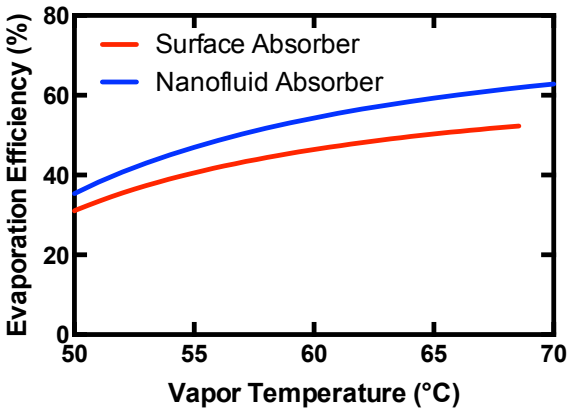

Figure S14: Comparison of surface and nanofluid absorber efficiencies for low temperature vapor generation.

S11. References

[1] T.L. Bergman, A.S. Levine, F.P. Incropera, D.P. Dewitt, Fundamentals of Heat and Mass Transfer, 7 ed., John Wiley & Sons, 2011.

[2] D.M. Kerslake, The Stress of Hot Environments, Reissue, Cambridge University Press, 2011.

[3] C.-Y. Su, A.-Y. Lu, Y. Xu, F.-R. Chen, A.N. Khlobystov, L.-J. Li, ACS Nano 5 (2011) 2332–2339.

[4] B.J. Stagg, T.T. Charalampopoulos, Combust. Flame 94 (1993) 381–396.

[5] Z. Fang, Y.-R. Zhen, O. Neumann, A. Polman, F.J. García de Abajo, P. Nordlander, N.J. Halas, Nano Lett. 13 (2013) 1736–1742.

[6] H. Ghasemi, G. Ni, A.M. Marconnet, J. Loomis, S. Yerci, N. Miljkovic, G. Chen, Nature Communications 5 (2014) 1–7.

[7] H.D. Downing, D. Williams, Journal of Geophysical Research (1975).

[8] O. Neumann, C. Feronti, A.D. Neumann, A. Dong, K. Schell, B. Lu, E. Kim, M. Quinn, S. Thompson, N. Grady, Proc. Natl. Acad. Sci. U. S. a. 110 (2013) 11677–11681.